Characterization of Ionic Liquid Ion Sources for Focused Ion Beam Applications

by

Carla S. Perez Martinez

B.S., Aeronautics and Astronautics, Massachusetts Institute of Technology

Submitted to the Department of Aeronautics and Astronautics in partial fulfillment of the requirements for the degree of

Master of Science in Aeronautics and Astronautics

at the

MASSACHUSETTS INSTITUTE OF TECHNOLOGY

June 2013

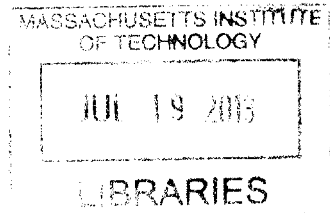

© Massachusetts Institute of Technology 2013. All rights reserved.

Author . . . .
Department of Aeronautics and Astronautics
May 23, 2013

Certified by . . . .
Paulo Lozano
Associate Professor
Thesis Supervisor

Accepted by . . . .
Eytan Modiano
Professor of Aeronautics and Astronautics
Chair, Graduate Program Committee

Characterization of Ionic Liquid Ion Sources for Focused Ion Beam Applications

by

Carla S. Perez Martinez

Submitted to the Department of Aeronautics and Astronautics
on May 23, 2013, in partial fulfillment of the
requirements for the degree of
Master of Science in Aeronautics and Astronautics

Abstract

In the Focused Ion Beam (FIB) technique, a beam of ions is reduced to nanometer dimensions using dedicated optics and directed to a substrate for patterning. This technique is widely used in micro- and nanofabrication for etching, material deposition, microscopy, and chemical surface analysis. Traditionally, ions from metals or noble gases have been used for FIB, but it may be possible to diversify FIB applications by using ionic liquids. In this work, we characterize properties of an ionic liquid ion source (ILIS) relevant for FIB and recommend strategies for FIB implementation.

To install ILIS in FIB, it is necessary to demonstrate single beam emission, free of neutral particles. Beams from ILIS contain a fraction of neutral particles, which could be detrimental for FIB as they are not manipulated by ion optics and could lead to undesired sample modification. We estimate the neutral particle fraction in the beam via retarding potential analysis, and use a beam visualization tool to determine that most of the neutral population is located at the center of the beam; the neutral population might then be eliminated using filtering. The same instrument is used to determine the transition of the source from single to multiple beam emission as the extraction voltage is increased. These studies should guide in the design of the optical columns for an ILIS-based FIB.

Thesis Supervisor: Paulo Lozano
Title: Associate Professor

Acknowledgments

I would like to thank my advisor, Professor Paulo Lozano. Since I stepped into his office all those years ago to get a UROP, I have received much knowledge, curiosity and excitement, but I have been taught most importantly in humbleness and kindness. I feel privileged to be one of his lab children.

Many thanks to Drs. Jacques Gierak and Stéphane Guilet for hosting me in France that summer and getting me excited about focused ion beams. I would like to thank Professor Manuel Martínez-Sánchez and Professor Sheila Widnall for their guidance, and Professor David Darmofal for being a terrific undergraduate advisor. I would also like to thank Dr. Jason Sanabia, Dr. John Notte, Dr. Mark Schattenburg and Professor Karl Berggren for their scientific advice.

Thank you to Dan Courtney, Tim Fedkiw and Anthony Zorzos, who advised me as an undergrad and made possible much of this work. Thanks to Todd Billings and David Robertson for all the technical support in fulfilling these experiments, and to Marilyn Good and Meghan Pepin for their support outside the lab. And thank you to UROP students Jennifer Quintana, Alex Feldstein and specially Jimmy Rojas for being such stars in the lab. Thank you also to all my lab mates for their help along the way.

Many thanks to the peers that have been so kind to me these years: my friends Bruno Alvisio, Agata Wisniowska, Lina Garcia, Nina Siu, Michael Lieu, Eric Dow, Vedran Sohinger, Elizabeth Qian, Adrienne Tran, Maria de Soria and Carmen Guerra. Thank you to Stanley and Connie Kowalski and Jose Pacheco and Letty García, for taking care of me and embracing me into their families.

I have been blessed above all things with my wonderful family. Muchas gracias, Mami, Papi, Mónica y Renato por todo su apoyo y su paciencia conmigo, por quererme tanto y por darme fuerzas todos los días. Gracias a mis tías, tíos, abuelas y primos por su cariño y su apoyo. Tanto amor es prueba que Dios no se deja vencer en generosidad. Esta tesis es de todos.

And many thanks and much love to Tom. Thank you for bearing with me in the

bumpy moments and for encouraging me to be a better scientist, I am so happy to have found you.

This research has been made possible by funds provided by the National Science Foundation and the Air Force Office for Scientific Research.

Contents

1 **Introduction** **15**
  1.1 Focused Ion Beam Overview and Applications 15
  1.2 Ion Sources for FIB 17
    1.2.1 Requirements 19
    1.2.2 Liquid Metal Ion Sources 20
    1.2.3 Gas Field Ionization Sources 22
    1.2.4 Other Ion Sources 25
  1.3 A new hope: Ionic Liquid Ion Sources 27

2 **Physics of Ionic Liquid Ion Sources** **31**
  2.1 ILIS Basic Physics 31
    2.1.1 Taylor Cone formation 31
    2.1.2 Ion Evaporation and Emission Site 34
    2.1.3 Starting Voltage 38
  2.2 ILIS performance in FIB 42
    2.2.1 Brightness and Energy Characteristics of ILIS Beams 42
    2.2.2 Probe Size Estimation and Preliminary Focusing 44
  2.3 Thesis Contributions 47

3 **Experimental Techniques** **49**
  3.1 Source Fabrication and Emitter-Extractor Setup 49
  3.2 Ion Beam Visualization 52
  3.3 Neutral Beam Visualization 54

3.4 Retarding Potential Analysis 55

4 Experimental Results **57**

4.1 Beam Visualization 57

4.1.1 Basic Beam Profile and Polarity Alternation Stability 57

4.1.2 Influence of the Applied Voltage 59

4.2 Neutral Beam Visualization 66

4.3 Retarding Potential Analysis 69

5 Conclusions and Future Work **73**

5.1 Implications of characterization results 73

5.2 Distal Electrode Configurations for long lifetime 75

5.3 The road to an ILIS-based FIB 76

List of Figures

1-1 FIB column outline, based on [9] 16

1-2 (a) FIB thinning of a sample to produce a sample for TEM inspection, from [9] (b) TEM lamella, from [21] 17

1-3 Schematic of Einzel lens chromatic aberration. Particles coming at different energies are deflected differently in the electric field generated within an Einzel lens 19

1-4 (a) LMIS basic setup (b) Gallium ion source in operation (from [9]) . 21

1-5 Basic GFIS setup 23

1-6 (a) Blunt GFIS tip, emitting many beamlets from ionization disks located above atoms (b) Beam pattern produced by GFIS (c) Super tip, emitting beamlets only from topmost atoms (d) Few beamlets produced by super tip [35] 24

1-7 (a) He Ion Microscope (left) vs. Scanning Electron Microscope images (right). Note the finer topography details in the HIM image. Both images have 20 μm field of view [35] (b) 5 nm ribbon patterned on graphene using He FIB [12] 25

1-8 (a) EMI-BF_4, $C_6N_2H_{11}^+BF_4^-$ Courtesy T. Coles (b) ILIS basic setup . 27

1-9 (a) Pure mechanical etching (b) Mechanical etching with reactive gas assistance (c) ILIS milling with reactive ions does not require gas assistance 28

1-10 (a) Experimental Setup for ILIS etching experiments (b) Si wafer after ILIS irradiation, with grid pattern transferred onto substrate 29

2-1 Diagram of a Taylor Cone. 32
2-2 Field Emission. (a) Image charge diagram (b) Potential due to image charge and electric field 35
2-3 (a) Emission site diagram (b) Liquid Vacuum interface and Gaussian pillbox 37
2-4 Prolate spheroidal coordinate system ($x = 0$ plane) 40
2-5 Diagram of break-up from n=1 to n=0 43
2-6 Probe Size and Probe Current Density for a hypothetical ILIS FIB . 45

3-1 Electrochemical Etching Setup 50
3-2 Scanning electron micrograph of ILIS tip after wetting with EMI-BF_4. 51
3-3 (a) Visualization setup diagram (b) Pictures of experimental setup . . 53
3-4 Visualization setup with deflector plates 54
3-5 Sample trajectories of EMI^+ for different deflection voltages. The entrance of the deflector is at x=0. 55
3-6 (a) RPA diagram (b) Picture of setup 56

4-1 Beam profiles for emission in alternating polarity. (a and b) Contour plots of beam profile in negative and positive mode, respectively. (c and d) Beam profile cross-section in negative and positive mode, respectively, with comparison to theoretical parabolic distribution. . . . 58
4-2 (a)-(f) Beam profiles for emitter voltages from $V_{app} = 1.1$ to $V_{app} = 1.7$ kV. We note that the profiles appear rounded off as the BVS has a circular imaging area; data appearing near $x = 0$ mm, $y = 40$ mm corresponds to reflections of light on the metal surrounding the imaging area. 60
4-3 (a)-(f) Beam profiles for emitter voltages from $V_{app} = -1.1$ kV to $V_{app} = -1.6$ kV. 61
4-4 (a)-(k) Beam profiles for emitter voltages from $V_{app} = 1$ kV to $V_{app} = 1.5$ kV 63

4-5 (a)-(k) Beam profiles for emitter voltages from $V_{app} = -1$ kV to $V_{app} = -1.5$ kV 64
4-6 Beam profiles for different emitter voltages for a larger R_c tip 65
4-7 Diagram of emitter with Taylor cone at (a) Starting voltage (b) Voltages for which multiple cones can be sustained 65
4-8 (a and b) Undeflected beam profiles (c and d) Profiles of neutral particles and deflected beam. 67
4-9 (a and b) Undeflected beam profiles (c and d) Profiles of neutral particles and deflected beam. 68
4-10 (a) Undeflected beam profile of a multiple cone emission (b) Multiple beams are deflected and neutral signal observed 69
4-11 Retarding Potential Analyzer Curves for $V_{app} = \pm 1.4$ kV 70

5-1 Schematic of possible filtering setup for ILIS FIB implementation . . 74
5-2 ILIS with the distal electrode configuration. From [1] 76

List of Tables

2.1 Probe sizes and current densities 46

Chapter 1

Introduction

Focused Ion Beam (FIB) systems have become ubiquitous in semiconductor manufacturing and in micro and nanofabrication. Commercial systems based on Liquid Metal Ion Sources (LMIS) and Gas Field Ionization Sources (GFIS) allow manufacturing and microscropy of materials down to the nanometer scale, but these technologies have some limitations that could be overcome by using a different source of ions. In this thesis, we focus on the development of Ionic Liquid Ion Sources (ILIS) as a new option for FIB systems, discuss the advantages these sources could bring, and perform some initial characterization required to optimize and implement ILIS in FIB.

In this chapter, we review the basics of FIB technology, the different ion sources technologies available, and introduce ILIS as a new and versatile option in FIB applications.

1.1 Focused Ion Beam Overview and Applications

In the FIB technique, a beam of ions is obtained from an ion source, and then directed to an optical column containing apertures, electrostatic lenses and deflectors, that narrow the beam to nanometer dimensions and direct it to a substrate for patterning, as shown in Fig. 1-1.

Focused ion beams have a number of uses in the semiconductor industry, in the fabrication of microelectromechanical systems, and in biological studies. FIB systems

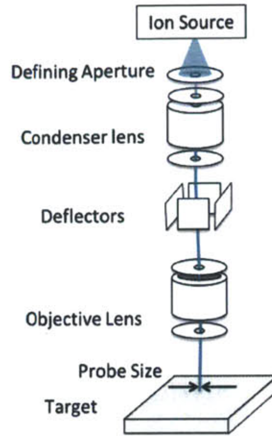

Figure 1-1: FIB column outline, based on [9]

are routinely used for micromachining applications, such as material removal due to sputtering of the incident ions, or material deposition, where a precursor gas reacts with the surface in the presence of the ion beam to produce a microstructure [24, 34]. A key application is circuit modification and repair, in which it is possible to edit integrated circuit connections by means of an ion beam. One of the areas where FIB has become indispensable is the preparation of samples for Transmission Electron Microscopy (TEM), where a sample must be thinned out to less than 100 nm in order to be electron transparent [9, 21]. The material around the sample is removed by FIB-induced sputtering. A schematic of the process and an example lamella are shown in Fig. 1-2.

FIB systems can also be used to analyze surfaces. When an ion impacts the surface, it has the effect of removing both ions and electrons from the surface. In Secondary Ion Mass Spectrometry, the ions ejected from the surface are used for chemical analysis, and since the ion beam removes material gradually from the sample, it is possible to profile the composition along the depth of the sample. Furthermore, the secondary electrons produced upon ion impact can be used for imaging. Recently, the Helium Ion Microscope (HIM), a FIB system based on a helium GFIS, has demonstrated sub-nm resolution and has been able to overcome some of the artifacts posed by traditional scanning electron microscopy [35].

FIB technology is extremely useful, but more research is needed in order to expand

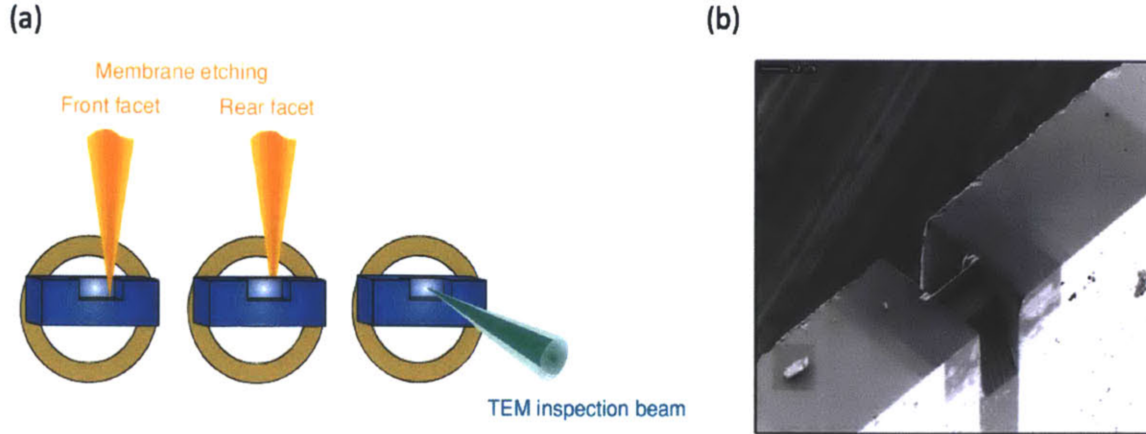

Figure 1-2: (a) FIB thinning of a sample to produce a sample for TEM inspection, from [9] (b) TEM lamella, from [21]

or improve the capabilities of current systems. We now give an overview of the different FIB systems based on the ion source type, by reviewing their advantages and their limitations. This thesis is concerned with the development of a new ion source for FIB, the ionic liquid ion source (ILIS), which is introduced at the end of the chapter.

1.2 Ion Sources for FIB

FIB systems strive for improvement of the probe size, which is defined to be the smallest diameter of the beam after focusing, while maintaining a current density in the probe that is high enough for the required application. The probe size d determines the resolution that can be patterned using a FIB system, and thus should be as small as possible. The probe size depends on several parameters from the ion source and the optical system, and can be calculated to be the contribution of the lens magnification on the source size and the contributions of chromatic and spherical aberrations of the optical system [24].

For a perfect, symmetric Einzel lens, the probe size would be simply given by the lens magnification M of the source size D:

$$d_D = MD \tag{1.1}$$

Lenses, however, have artifacts that increase this theoretical size. A lens focuses particles that are coming further from its optical axis more strongly than the particles coming close to it, an effect known as spherical aberration. The spherical aberration depends on the current accepted from the beam, I (note this might be different than the current emitted from the source, as we may limit the current accepted into the optical system using defining apertures, see Fig. 1-1), as well as on the current angular spread $\frac{dI}{d\Omega}$, where Ω is the unit solid angle. We assume a constant $\frac{dI}{d\Omega}$ for this analysis. The spherical aberration also depends on the lens magnification and the lens spherical aberration coefficient C_s, and its contribution to the probe size is given by

$$d_s = \frac{I^{3/2}}{2} \frac{C_s^2}{[\pi M^2 \frac{dI}{d\Omega}]^{3/2}} \tag{1.2}$$

Chromatic aberration is also an important contribution to the probe size. Einzel lenses traditionally used for FIB will focus a particle depending on the particle's energy, so if particles come at different energies from each other, the lens will focus them on a different spot, giving in a larger beam size, as shown in Fig. 1-3. Ideally, an ion source emits all particles at an energy W. However, due to the physics of ion emission, some particles come at energies slightly different from the main energy peak. Let $\Delta W_{1/2}$ be the full-width-at-half-maximum of the energy distribution. The chromatic aberration contribution to the probe size is given by

$$d_c = I^{1/2} \left(\frac{\Delta W_{1/2}}{W} \right) \frac{C_c}{[\pi M^2 \frac{dI}{d\Omega}]^{1/2}} \tag{1.3}$$

where C_c, the chromatic aberration aberration coefficient, quantifies the spreading effect for a given lens. Adding up the contributions from equations 1.1, 1.2, and 1.3 in quadrature, the probe size is given by

$$d^2 = \frac{I^3}{4} \frac{C_s^2}{[\pi M^2 \frac{dI}{d\Omega}]^3} + I \left(\frac{\Delta W_{1/2}}{W} \right)^2 \frac{C_c^2}{[\pi M^2 \frac{dI}{d\Omega}]} + M^2 D^2 \tag{1.4}$$

From 1.4, we observe that reducing the current will lead to a smaller probe size, but doing so is not always practical. Some applications, such as material removal, require high current densities in the sample in order to reduce the processing time,

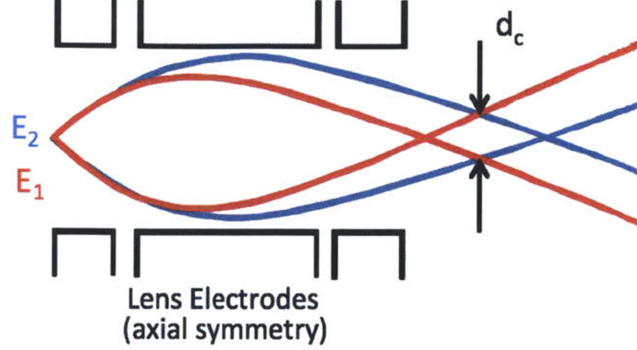

Figure 1-3: Schematic of Einzel lens chromatic aberration. Particles coming at different energies are deflected differently in the electric field generated within an Einzel lens

and in microscopy, having higher currents improves the signal available for image acquisition. Thus, it becomes necessary for the source to have optical properties that will favor a smaller probe size without resorting to current reductions. We enumerate some of the requirements an ion source must satisfy in order to be implemented in a FIB system reliably and with sub-micrometer probe size, before numbering the sources available.

1.2.1 Requirements

The following properties of an ion source measure its viability in a FIB system:

- **High Brightness**. An ion source produces a current I_b from a source size D and sprays it into a cone with half angle α_0, or into a solid angle $\Omega = 2\pi(1 - \cos\alpha_0) \approx \pi\alpha_0^2$. The brightness of the source is a measure of how tightly we can confine the current of the ion beam, and is given by

$$\beta = \frac{4I_b}{(\pi\alpha_0 D)^2} \tag{1.5}$$

  Brightness affects the probe size through the beam angular spread, current density and source size. The higher β, the better probe size and current that can be achieved; it is usually required that a source has $\beta > 10^6 \mathrm{Acm^{-2}sr^{-1}}$ [12].

- **Energy Spread**. From equation 1.4 it is evident that the smaller the energy spread, the better the resolution of the FIB system. The value of $\Delta W_{1/2}$ must be minimized [32], and should be restricted to less than 10 eV.

- **Lifetime**. FIB systems are very complex machines with high-vacuum systems, specimen stages and delicate optics. It is desirable for a source to have lifetimes greater than hundreds of hours in order to minimize source replacement and the exposure of these systems to contamination.

- **Beam Stability**. The beam from an ion source must be "precisely in relation with the elements of an optical system" [22] for adequate focusing, which means that the beam should not drift during operation. Furthermore, we require the current emitted should be constant to within 1-2% over periods of several minutes, so that there are no variations at different points in the scan during the patterning process.

There are a few ion source candidates for FIB operation, and we discuss LMIS and GFIS in detail, as they are used in commercially available systems capable of sub-100 nm patterning. Other less popular ion sources are also discussed.

1.2.2 Liquid Metal Ion Sources

LMIS are the most widely used sources for FIB, due to their high-brightness and reliability [9]. The ion production mechanism in LMIS is field evaporation from liquid metals. To achieve ion evaporation, a tungsten tip that has been sharpened to a radius of curvature of $\sim 10\ \mu$m is covered with a molten liquid metal. The tip, or emitter, is in contact with a liquid reservoir. The tip is placed in front of a metallic plate with an aperture in it, the extractor, as shown in Fig. 1-4. The emitter extractor assembly is placed in vaccum. By applying a potential difference of 10 or more kV between the emitter and the extractor, the electrostatic pressure overcomes the surface tension forces on the liquid, and the liquid surface evolves into a conical structure known as a Taylor cone [31]. At the apex of the Taylor cone, the electric

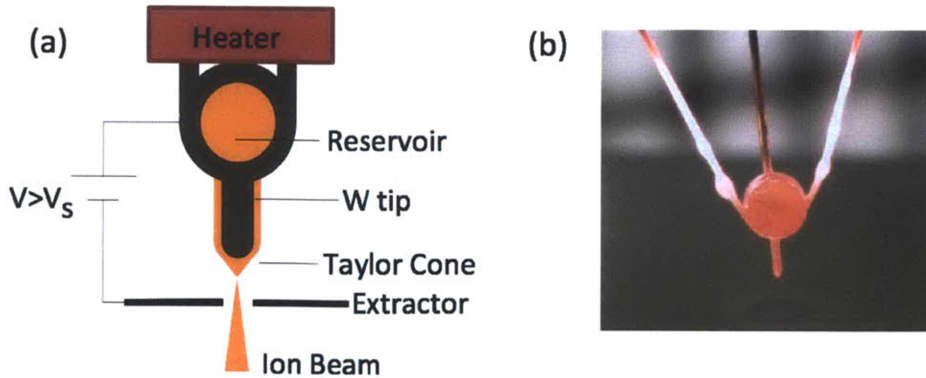

Figure 1-4: (a) LMIS basic setup (b) Gallium ion source in operation (from [9])

field is of the order of several V/nm, which triggers direct ion evaporation from the liquid surface.

Several ion species can be produced from LMIS, although the list of available species is limited. Metals used in LMIS must have low vapor pressures for vacuum operation as well as low melting points, since operation at high temperatures can lead to reactions with the substrate and also promote the evaporation of neutrals. Sources capable of producing Ga, In, Bi, Al, Sn, Cs, and Au have been demonstrated. It is possible to obtain other elements including B, As, Si, Ge, and Pt if an alloy source is used, in which case the optical column will contain a Wien filter that separates and selects ion species based on their masses [24]. By far, the most widely used source in FIB is the Ga^+ LMIS.

Ga^+ LMIS have attributes that allow them to be routinely focused to sub-100 nm dimensions [9]. They emit currents of several μA, although they are usually operated at 2 μA in order to minimize the energy spread, which increases at higher currents. The minimum energy spread is 5 eV. At this current, the source has a current angular spread of 20 μAsr^{-1}. The ion emission area at the apex of the Taylor cone is approximately 5 nm in diameter, but due to space charge effects from the high current density near the emission site, the beam spreads through Coulombic interaction, and the effective emission site is 50 nm in diameter. Using these values, LMIS brightness is estimated to be 10^6 $\text{Acm}^{-2}\text{sr}^{-1}$. The smallest probe size demostrated, using state-of-the-art optics, is 5 nm [9].

Ga^+ LMIS FIB systems have become a tool for creating nanostructures through both substractive and additive processes. The large sputter yield [1] of Ga^+ ions allows removing material for patterning of nanoscale holes, arrays and channels [33]; the beam can also be used to perform 3D milling not accesible to other methods like conventional optical lithography [8]. Ga^+ beams can also be used to perform ion implantation and growth of 3D structures with ion induced deposition.

Despite their widespread use, Ga^+ FIB systems have key limitations. When patterning at scales below 30 nm, the focused beam has tails that perform undesired modification in the edges of the fine structures being created. In addition, use of Ga^+ ions can lead to sample contamination, which is not acceptable in some applications; Ga^+ contamination can affect both electrical and magnetic properties of a device [32].

1.2.3 Gas Field Ionization Sources

Gas Field Ionization Sources produce beams of ions from noble gases by virtue of field ionization [22]. The basic GFIS setup is shown in Fig. 1-5. A sharpened tungsten needle, with a radius of curvature of $\sim$ 100 nm, is placed in front of an extractor. A voltage difference of a few kV is applied between the emitter and the extractor, so that fields in the order of 10 V/nm are achieved at the tip. A gas (usually noble) is introduced near the tip, in order to supply the particles to be ionized. The emitter must be cooled cryogenically in order to increase the density of atoms available for ionization. Once an atom is in the vicinity of the tip, it is possible for the atom to be ionized by quantum mechanical tunneling of the electron into the metal, as the energy barrier has been distorted by the electric field. The resulting positive ions are accelerated away from the tip by the electric field. Several ion beams are obtained, one from each emitter atom involved in ionization.

FIB systems using GFIS had been demonstrated in the 1970s by the group led by Levi-Setti [4] and Orloff and Swanson [23]. Probe sizes of 50 nm with current densities of 10 pA were demonstrated [24]. Nonetheless, these ions sources were difficult to

[1] Sputtering yield is defined as the ratio of the number of atoms removed from the sample to the number of incident ions

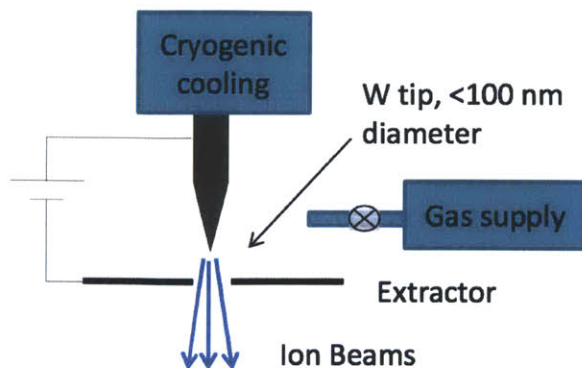

Figure 1-5: Basic GFIS setup

maintain, had current fluctuations if any impurities were present in the source gas, and the current densities achievable were too low in comparison with the LMIS, so they were not implemented widely in FIB [32]. Recently, however, improvements in the tip construction and geometry have allowed implementation of these sources in FIB systems.

In a generic GFIS, the tip is roughly a few hundreds of atoms in diameter, and the ionization of the gas is distributed between all these atoms, as shown in Fig. 1-6. However, by sharpening the tip to be only three atoms at the apex, it is possible to concentrate the total gas supply to these three atoms instead of the hundreds of atoms in the blunter tip [35]. Such a tip can be produced reliably and can last months in operation. Using He, the source produces three main beamlets, of which one is selected for focusing. The source size is approximately 3 Å, and the current density is 2.5 μAsr^{-1}, giving a brightness of $4 \cdot 10^9$ Acm^{-2}sr^{-1}. In addition, the source has an energy spread of less than 1 eV; these properties allow it to be focused to an ultimate spot size of 0.25 nm. This improved He^+ source has been implemented in FIB as an ultra-high resolution microscopy tool. Scanning electron microscopes have probe sizes of down to 1 nm, but incident electrons will interact with the sample through an extended volume and produce signals from an area larger than the probe size. Helium ions, with a much larger mass, will keep going straight through the sample and have a smaller interaction volume, thus producing signals from a smaller area than electrons would, and giving images with improved resolution (Fig. 1-7(a)).

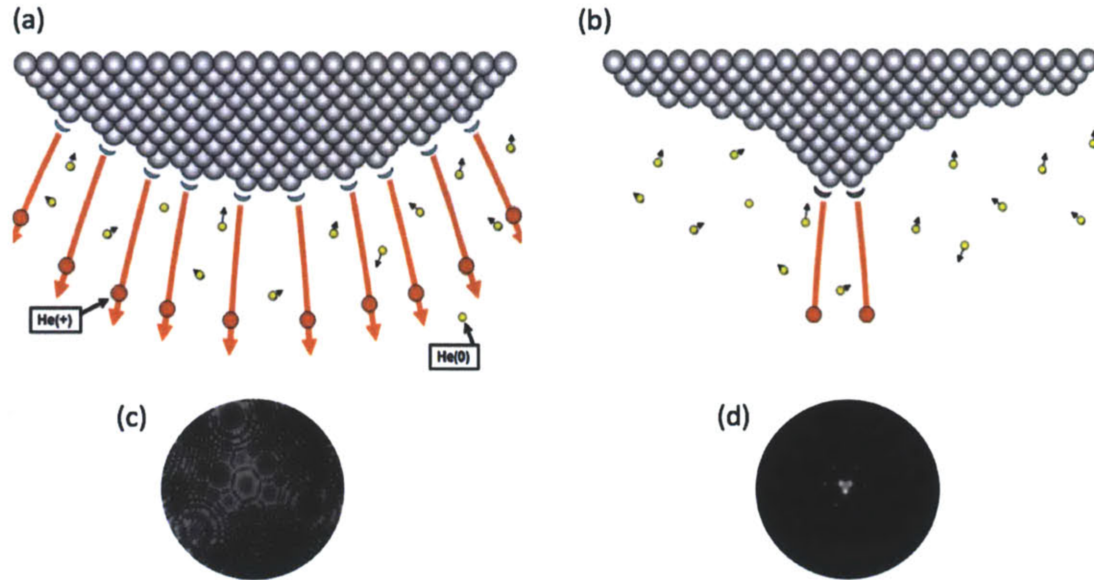

(c) (d)

Figure 1-6: (a) Blunt GFIS tip, emitting many beamlets from ionization disks located above atoms (b) Beam pattern produced by GFIS (c) Super tip, emitting beamlets only from topmost atoms (d) Few beamlets produced by super tip [35]

Furthermore, helium ions can be used to pattern materials at scales not accesible by LMIS; it is much easier to produce sub-10 nm structures using a He^+ beam than Ga^+, as Ga^+ FIB require dedicated optics to achieve the smallest probe sizes, and because of the Ga^+ beam tail effects explained above. An example of patterning in graphene by He^+ is shown in Fig. 1-7(b).

Despite their resolution capabilities, He^+ systems are limited in their throughput for machining applications, as the current achieved in the probe cannot exceed 30 nA, and because He^+ ions are not as efficient as Ga^+ in material removal. Neon, which should be more effective than Helium in sputtering due to its larger mass, has also been introduced in a GFIS and used for sub-10 nm lithography [36]. Neon ions are still less effective than Ga^+ in sputtering, and the Ne^+ technology is incipient. GFIS FIB systems are also complex, as they require both cryogenic cooling, high-purity gases and ultra-high vacuum operation.

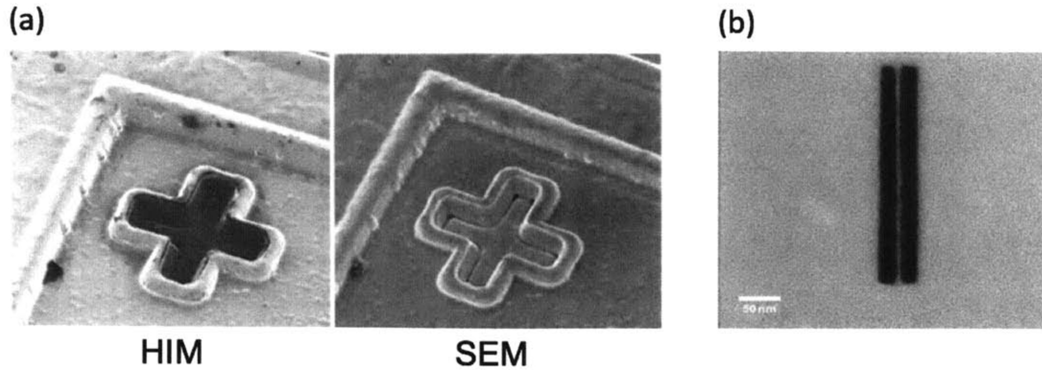

Figure 1-7: (a) He Ion Microscope (left) vs. Scanning Electron Microscope images (right). Note the finer topography details in the HIM image. Both images have 20 μm field of view [35] (b) 5 nm ribbon patterned on graphene using He FIB [12]

1.2.4 Other Ion Sources

Ion sources of lower brightness and energy spreads than LMIS and GFIS have been mentioned in the literature, and although they cannot reach the same level of resolution of the two sources we have discussed, they can be of advantage in applications requiring rapid milling or other ion species. We mention three plasma ion sources and an electrolyte ion source:

- **Inductively Coupled Plasma (ICP) Source**. In ICP sources, a plasma is created inductively by an RF antenna, and ions are extracted from the plasma chamber through an aperture of 200 μm in diameter [30]. Beams of Ar^+ can be produced, with a brightness of 4590 $Acm^{-2}sr^{-1}$ and an energy spread of 7 eV, as well as Xe^+ beams with brightness of 10500 $Acm^{-2}sr^{-1}$ and spread of 10 eV. These sources have current densities of several mA sr^{-1}, considerably larger than those of Ga^+ LMIS, but the low value of the brightness results from the effective source size of $\sim$ 10 μm. ICP sources cannot compete with the Ga^+ LMIS in producing small beam sizes, although ICP sources are capable of producing sub-100 nm probes, albeit at limited probe currents. ICP sources do become useful, however, if probe sizes of several hundreds of nm are desired (for instance, for removal of bulk material). In this case, the ICP can give much larger current densities than a Ga^+ LMIS thanks to the superior current emitted. The larger current density, coupled with the sputter yield of heavy

ions like Xe^+, is beneficial for rapid milling applications. Furthermore, ions like Ar^+ or Xe^+ do not have the same issues with contamination as Ga^+.

- **Multicusp Plasma Ion Source** A source of this type was described by Scipioni et al. [29]. A plasma is formed in a 50 cm^3 volume by a filament discharge, with electrons confined by a multicusp magnetic field, and the ion beam exits through a 1 mm diameter aperture. Beams of inert ion species such as Kr^+, Ne^+, and He^+ have been produced by this source, although their brightness does not exceed 2000 $Acm^{-2}sr^{-1}$ and so sub-100 nm probes are impractical.

- **Penning Type Plasma Ion Source** Guharay et al. [10] developed a Penning surface plasma source capable of producing both positive or negative ions. The authors report H^- beams with brightness of $5 \cdot 10^4$ $Acm^{-2}sr^{-1}$, with less than 3 eV energy spread. This source has the unfortunate need for pulsed operation and has not been developed further, but is one of the few ion sources of relatively high-brightness capable of producing negative ion species, which, as will be explained later, could be beneficial for applications where charging of samples is not desired.

- **Solid Electrolyte Ion Sources** Escher et al. [3] demostrated an ion source based on the solid electrolyte $(AgI)_{0.5}(AgPO_3)_{0.5}$. In the solid electrolyte, mobile ions (such as Ag^+ for Escher's source) can move freely; by shaping the electrolyte as a sharp tip and placing it in front of a metallic extractor, it is possible to extract the mobile species by applying a voltage difference of several kV. The source tested by Escher et al. could sustain μA over several days. These sources have not been developed further, but could potentially provide many other species, such as Cu^+, F^-, O^{2-} and H^+, by choosing an appropriate electrolyte.

From this survey of ion sources for FIB, it is clear that although several ion species are accessible, there is a need to develop ion sources of brightness comparable to LMIS, capable of providing a greater variety of ion species, especially negative ions.

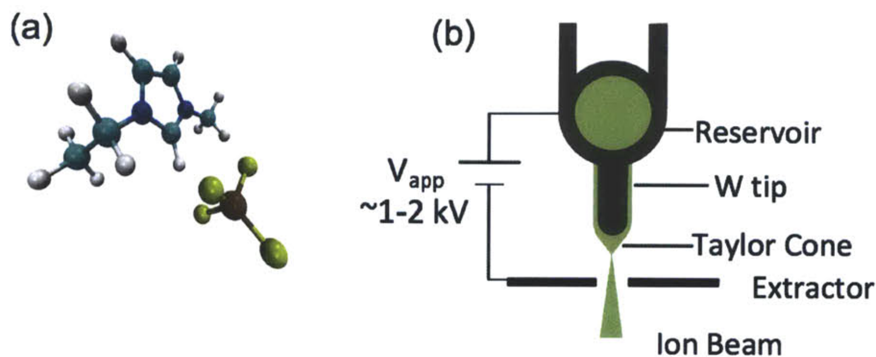

Figure 1-8: (a) EMI-BF_4, $C_6N_2H_{11}^+BF_4^-$ Courtesy T. Coles (b) ILIS basic setup

1.3 A new hope: Ionic Liquid Ion Sources

Ionic Liquid Ion Sources have been recently proposed as a new tool for FIB [19, 37, 6]. ILIS are very similar to LMIS, but instead of relying on the field evaporation from liquid metals, ILIS beams are obtained from field evaporation of ionic liquids, or room-temperature molten salts. These substances are a mixture of complex organic and inorganic ions, which have negligible vapor pressures, making them apt for operation in vacuum. In addition, ionic liquids have high conductivities and low surface tensions, which make them capable of being electrostatically stressed into a Taylor cone to obtain ion evaporation. An example ionic liquid, EMI-BF_4, 1-ethyl-3-methylimidazolium tetrafluoroborate, is shown in Fig. 1-8(a).

The ILIS consists of an electrochemically sharpened tungsten needle–the emitter–coated with an ionic liquid (Fig. 1-8(b)). As in LMIS, the emitter is placed in front of a downstream metallic extractor, and a potential difference of 1-2 kV is applied between the emitter and the extractor in order to stress the liquid meniscus into a Taylor cone, from which ion emission is obtained.

ILIS have several key novelties that could be beneficial in FIB processes:

1. ILIS are capable of producing either positive or negative ion beams, by simply reversing the polarity of the applied potential. Negative ion beams can be of advantage in applications where the target is a dielectric sample; when a sample is irradiated with an ion beam, secondary electrons will be emitted from it. As a result, a non-conductive sample starts charging positively. If irradiated

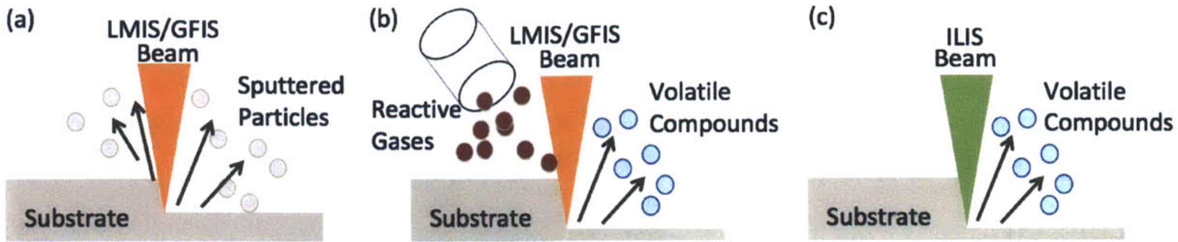

Figure 1-9: (a) Pure mechanical etching (b) Mechanical etching with reactive gas assistance (c) ILIS milling with reactive ions does not require gas assistance

with positive beams, the sample will charge even more positively. This charging results in the creation of a local electric field that will distort the incoming ion beam, and therefore blur the pattern being written. If using negative beams, the charging issue can be alleviated without the need for electron flooding systems that are usually used to compensate for positive charging with other FIB systems.

2. ILIS have the potential of producing a completely new selection of ion species, for example heavy molecular ions and reactive ions, as there are many ionic liquids described in the literature that could be used in ILIS. If using reactive ions in etching applications, a combination of physical erosion from the incident ions with chemical reactions at the surface could enhance the etching rates. In FIB, it is common practice to introduce reactive gases such as XeF_2 near the specimen. The gases react readily with the surface under the ion beam influence, create volatile species that aid in material removal, and therefore accelerate the milling process. This is depicted in Fig. 1-9 (a),(b). If using ILIS beams with reactive species such as I^-, BF_4^- and Cl^-, there is no need for introducing reactive gases in the chamber to achieve large milling rates (Fig. 1-9(c)).

It has been demonstrated that beams obtained from the liquid EMI-BF_4 are capable of etching silicon at rates faster than typical Ga^+ mechanical sputtering. A silicon wafer covered with copper grids was irradiated with an ILIS beam at 15 keV landing energy; after removing the copper grids, which acted as masks, the pattern was transferred to the silicon substrate (Fig.1-10). The sputtering

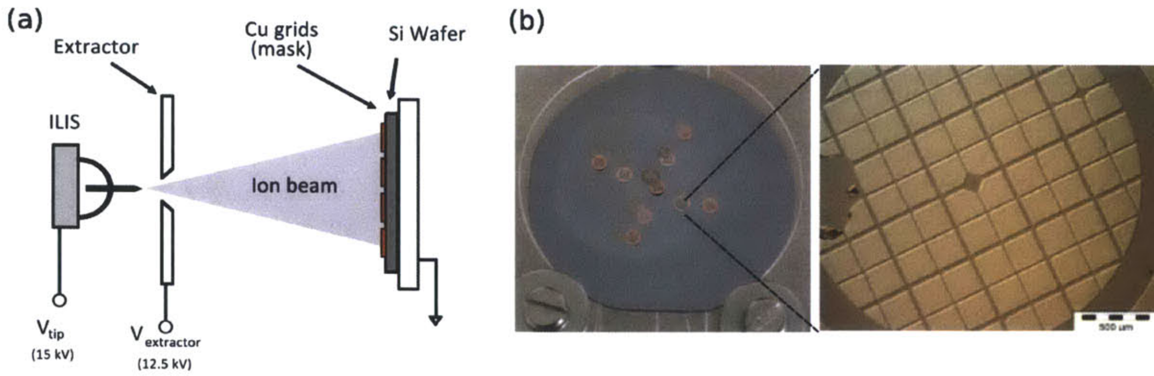

Figure 1-10: (a) Experimental Setup for ILIS etching experiments (b) Si wafer after ILIS irradiation, with grid pattern transferred onto substrate

yield was measured to be from 5 to 35 atoms of silicon removed per incident ion, compared to yields of 2 for Ga^+ ions at the same energy. [26]

3. ILIS operation is simpler than LMIS/GFIS, as ILIS emit at room temperature with no need for ultra-high vacuum.

These novelties should make ILIS ideal candidates for FIB utilization. In the next chapter, we will discuss in detail the physics of electrospray emission from ionic liquids. We will also mention the optical properties of ILIS relevant for FIB and previous work related to ILIS-FIB development.

Chapter 2

Physics of Ionic Liquid Ion Sources

In this chapter, we provide a review of the physics of ion production in ILIS and discuss the optical properties of ILIS relevant for FIB. We revisit Taylor cone formation, review the Schottky model of ion evaporation and derive a simple model of the emission site. We then mention brightness estimates for ILIS and give a review of the energy distributions of these sources. The chapter ends with a discussion of the probe sizes that could be reached by an ILIS based FIB.

2.1 ILIS Basic Physics

2.1.1 Taylor Cone formation

When the interface between an electrically conducting liquid and an insulator (often air or a vacuum) is charged electrically beyond a certain critical level, it becomes unstable and evolves from a rounded meniscus to a stable conical structure known as a Taylor cone [7]. It is possible to gain insight into the shape of the cone and the electric field distribution through a simple analysis.

We first solve for the electric field at the surface of the cone. Consider a cone of half-angle θ_T, with the origin at the apex of the cone, as shown in Fig. 2-1. We consider three stresses that act on the liquid: (1) the hydrostatic pressure difference with the medium, (2) the surface tension pressure and (3) the electric field stresses.

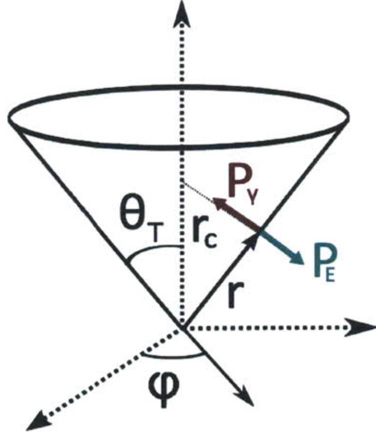

Figure 2-1: Diagram of a Taylor Cone.

Let Δp be the pressure difference between the liquid and the surrounding medium. The pressure due to surface tension is given by $P_\gamma = \gamma\kappa$, where γ is the surface tension of the liquid, and κ is the surface curvature. A distance r from the apex of the cone, κ is given by

$$\kappa = \frac{1}{r_c} = \frac{\cot\theta_T}{r} \tag{2.1}$$

The liquid is assumed to behave as a perfect conductor, i.e., the relaxation time has transcurred ($\sim$ 0.1 ns for an ionic liquid), so that all free charges have migrated to the surface of the conductor. The electric field is normal to the surface of the cone and zero inside the cone. With this assumption, the electrical pressure on the surface of the cone is given by the normal component of the Maxwell stress tensor, $P_E = \frac{1}{2}\epsilon_0 E_n^2$.

Balancing stresses, we obtain

$$\frac{1}{2}\epsilon_0 E_n^2 + \Delta p - \frac{\gamma\cot\theta_T}{r} = 0 \tag{2.2}$$

We assume we have no active pressure feed to the liquid, and we will assume that there are no pressure drops along the liquid due to viscosity effects. If we have no active pressure feed to the liquid (i.e. $\Delta p = 0$), the electric field along the surface of

the liquid is given by

$$E_n = \sqrt{\frac{2\gamma \cot \theta_T}{\epsilon_0 r}} \tag{2.3}$$

We proceed to find the electric field around the Taylor cone. If we assume no space charge in the region surrounding the cone, the electric potential Φ must satisfy Laplace's equation:

$$\nabla^2 \Phi = 0 \tag{2.4}$$

In our axisymmetric problem, there is no dependence on the azimuthal coordinate ($\frac{\partial}{\partial \phi} = 0$), and this equation 2.4 reduces to

$$\frac{1}{r^2}\frac{\partial}{\partial r}\left(r\frac{\partial \Phi}{\partial r}\right) + \frac{1}{r^2 \sin\theta}\frac{\partial}{\partial \theta}\left(\sin\theta \frac{\partial \Phi}{\partial \theta}\right) = 0 \tag{2.5}$$

The solution to equation 2.5 is a combination of functions including Legendre functions Q_ν, P_ν,

$$\Phi = \sum_\nu \left(A_\nu Q_\nu(\cos\theta) r^\nu + B_\nu P_\nu(\cos\theta) r^\nu\right) + \Phi_0 \tag{2.6}$$

Here, ν can be any real number, A_ν and B_ν are constant coefficients, and Φ_0 is a constant potential dependent on boundary conditions. We note that P_ν has a singularity for $\theta = \pi$; as this is a region of free space where the potential should be finite, we must impose $B_\nu = 0 \;\forall\; \nu$. This potential solution should also be consistent with the electric field at $\theta = \theta_T$, which requires

$$E_n = -\frac{1}{r}\frac{\partial \Phi}{\partial \theta} = \sum_\nu A_\nu Q_\nu' r^{\nu - 1} = \sqrt{\frac{2\gamma \cot\theta_T}{\epsilon_0 r}} \tag{2.7}$$

From here, we find that the only Legendre function permitted is that corresponding to $\nu = 1/2$, which implies the potential is of the form

$$\Phi(r, \theta) = A_{1/2} Q_{1/2}(\cos\theta) r^{1/2} + \Phi_0 \tag{2.8}$$

As we had considered the liquid to be a perfect conductor, the $\theta = \theta_T$ surface must be an equipotential surface. From (2.8), it is evident that Φ will have some variation

through r unless $Q_{1/2}(\cos\theta_T) = 0$, which occurs for a cone half-angle of 49.29°. We note that this half-cone angle is independent of the liquid or the applied potentials.

This analysis predicts well the shape of observed electrified menisci, but it is not an exact treatment. The solution for the field in equation (2.3) has a singularity at $r = 0$, which is not physical. The equilibrium breaks close to the apex of the cone, and emission of charged particles under different regimes can occur depending on the liquid conductivity or on the flow rates supplied to the cone. The most-studied of these regimes is the cone-jet regime, in which the apex of the Taylor cone deforms into a thin jet that eventually breaks apart into a spray of charged drops and ions [7]. However, if the conductivity of the liquid is high or the flow rate of liquid to the cone is small, the jet size is reduced, and eventually it is possible to eliminate the jet and obtain pure ionic emission with no intervening droplets. This is the case for Taylor cones from liquid metals, and for ionic liquids.

In 2003, Romero-Sanz et al. [28] demonstrated pure ionic emission at low flow rates from a capillary emitter using the ionic liquid EMI-BF_4. Later on, Lozano and Martinez-Sanchez [17] obtained ionic emission from the same liquid using externally-wetted tungsten emitters, which came to be Ionic Liquid Ion Sources. Larriba et. al used this geometry to produce beams of ions from other ionic liquids [13], and so far every ionic liquid tested with this configuration has produced beams of ions with no intervening droplets.

In this thesis, we will only discuss ion evaporation, as ILIS operate in the purely ionic regime. Information on the cone-jet regime can be found elsewhere [7].

2.1.2 Ion Evaporation and Emission Site

In ILIS, we have evaporation of ions from a region close to the apex of the cone. For FIB, it is important to know the size of the emission site and the corresponding current in order to estimate the brightness of the source, and to find this, we require the critical electric field required for ion evaporation. This field can be found via Schottky's model, which we review in this section. Having the field, we proceed to estimate the emission site size and the associated current.

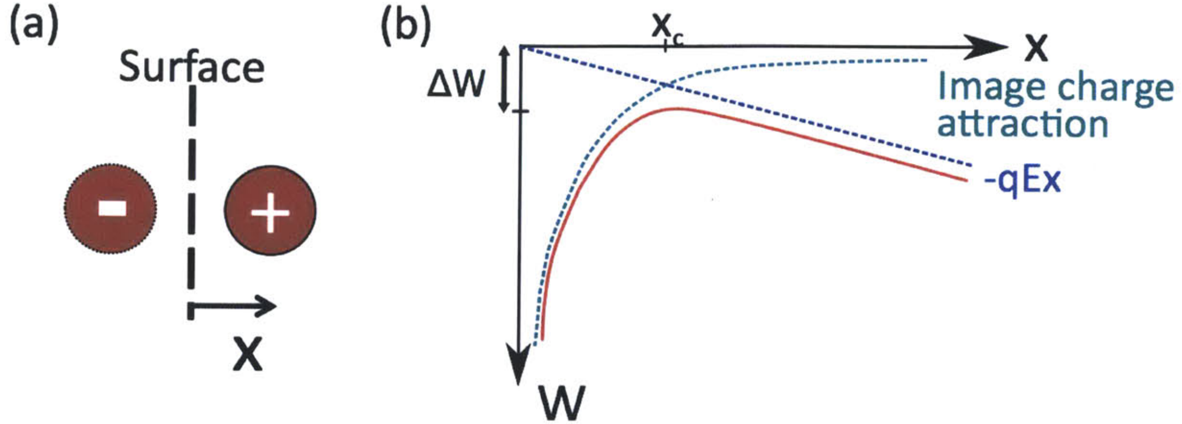

Figure 2-2: Field Emission. (a) Image charge diagram (b) Potential due to image charge and electric field

We first consider a liquid-vacuum interface with no external electric field. The rate of evaporation of ions is given by the Richardson-Dushman law,

$$j = \sigma \frac{kT}{h} \exp\left(-\frac{\Delta G}{kT}\right) \tag{2.9}$$

where σ is the surface charge density, k is Boltzmann's constant, h is Planck's constant, T is the temperature, and ΔG is the energy barrier for ion evaporation, which is of the order of 1-2 eV for an ionic liquid [18]. At room temperature, the rate of ion evaporation is negligible, but it is possible to enhance it by applying an external electric field.

Let E be the externally applied electric field. We will consider the case of a positive ion of charge q evaporating from the liquid, although the argument is analogous for the negative ion case. The positive ion will experience two forces, the first an attraction towards the liquid from its image charge (see Fig. 2-2(a)), and the other the pull of the electric field away from the interface. A distance x away from the interface, the force felt by the ion is given by

$$\vec{F} = \left(qE - \frac{q^2}{4\pi\epsilon_0(2x)^2}\right)\hat{i}_x \tag{2.10}$$

The potential energy corresponding to this force is the sum of the potential due to the electric field and the potential due to the image charge, as shown in Fig. 2-2b,

and is given by

$$W = -qEx - \frac{q^2}{16\pi\epsilon_0 x} \tag{2.11}$$

From the potential energy diagram, we see that once the ion reaches a critical distance x_c, the attractive force is overcome by the electric field pull, and the ion effectively escapes from the attractive potential. The potential barrier is effectively lowered by an amount $\Delta W = -W(x_c)$, thanks to the prescence of the electric field. The critical distance can be found by maximizing 2.11, giving

$$x_c = \sqrt{\frac{q}{16\pi\epsilon_0 E}} \tag{2.12}$$

$$\Delta W = -W(x_c) = \sqrt{\frac{q^3 E}{4\pi\epsilon_0}} \tag{2.13}$$

Coming back to the Richardson-Dushman law, the energy barrier for evaporation is now $\Delta G - \Delta W$, giving

$$j = \sigma\frac{kT}{h}\exp\left(-\frac{1}{kT}\left(\Delta G - \sqrt{\frac{q^3 E}{4\pi\epsilon_0}}\right)\right) \tag{2.14}$$

Equation 2.14 is known as the Schottky Emission model. We can see that for small electric fields the evaporation rate is limited, but once we exceed a critical field

$$E^* = \frac{4\pi\epsilon_0 \Delta G^2}{q^3} \tag{2.15}$$

copious ion emission can be obtained. Taking q equal to the elementary charge and $\Delta G = 1.5$ eV, we find $E^* \approx 1.56$ V/nm. This means that, once we reach $E_n = E^*$, ions can be produced from the Taylor cone.

Ion emission will occur from a small region surrounding the apex, as shown in Fig. 2-3a. Let r^* be the characteristic radius of the emission region. It is possible to solve for r^* through the pressure equilibrium on the surface. However, in finding the electrostatic stresses, we cannot assume that the liquid behaves as a perfect conductor in this region, as charges are being removed from the surface and the liquid might

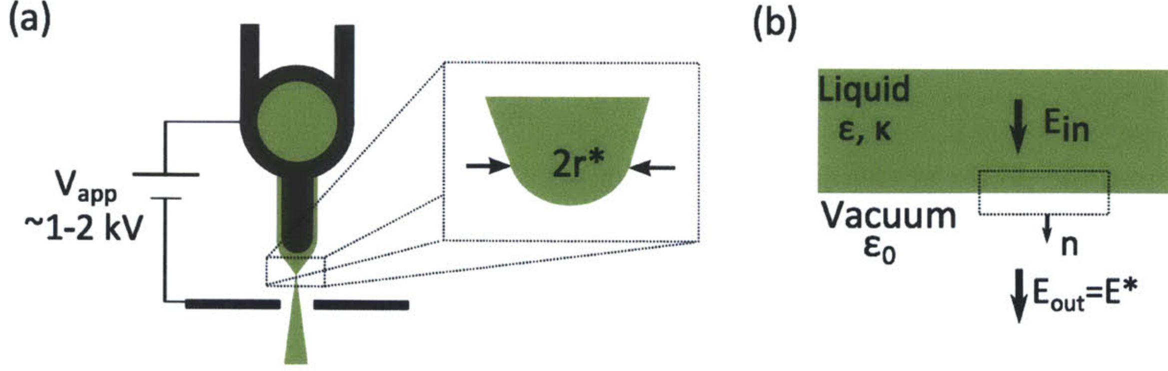

Figure 2-3: (a) Emission site diagram (b) Liquid Vacuum interface and Gaussian pillbox

not fully relax.

Let us take the electric field just outside of the evaporation region to be equal to the field required for ion evaporation, E^*, as shown in Fig. 2-3b. The internal electric field normal to the surface is E_{in}; any contributions from tangential electric fields are neglected for this analysis. If we integrate Gauss' Law for an infinitesimally thin pillbox with boundaries along the vacuum and the liquid, the following relation for the internal and external electric fields must hold:

$$\epsilon_0 E^* - \epsilon\epsilon_0 E_{in} = \sigma \tag{2.16}$$

where ϵ is the dielectric constant of the liquid and σ is the surface charge density on the interface. In the regions of the liquid where there is no evaporation, the surface charge must be $\epsilon_0 E_n$ and the internal electric field is zero, as the liquid behaves as a conductor; however, in the evaporation region, the surface charge must be greatly reduced by the charge removal, and the internal electric field must be significant. Therefore, we neglect the right hand side of equation 2.16, and approximate E_{in} as E^*/ϵ. The force balance on the surface of the evaporation region is now

$$\frac{1}{2}\epsilon_0 E^{*2} - \frac{1}{2}\epsilon\left(\frac{E^*}{\epsilon}\right)^2 = \frac{2\gamma}{r^*} \tag{2.17}$$

which implies

$$r^* = \frac{4\gamma}{\epsilon_0 E^{*2}} \left(\frac{\epsilon}{\epsilon - 1} \right) \tag{2.18}$$

If we take $E^* = 1.56 \cdot 10^9$ V/m, $\epsilon \sim$ 10, and $\gamma = 0.0452$ N/m [14] (approximate values for EMI-BF_4), we find $r^* \sim$ 10 nm. Although this value is an approximation, it indicates that ILIS could have competitive brightness for FIB.

We can also use this analysis to estimate the current produced by an ILIS. Let us suppose that the beam current corresponds to the liquid carried by conduction inside the meniscus. The current density is then $j = kE_{in} = kE^*/\epsilon$, where k is the conductivity of the liquid. If we assume that the current density constant is in the semi spherical cap from which emission occurs, the current is

$$I = 2\pi r^{*2} k \frac{E^*}{\epsilon} \tag{2.19}$$

Using $k \approx 1$ Si/m, which is the conductivity of EMI-BF_4 at room temperature, the current is estimated to be 85 nA. This value is slightly below the currents measured, which are of the order 100s of nA for operation at room temperature. There can be several reasons for this discrenpacy; Higuera [11] notes that the temperature could increase locally at the emission site due to ohmic dissipation, which would further increase the conductivity of the liquid. Furthermore, this analysis ignores the effects of convenction within the meniscus as well as the effects of concentration gradients near the emission site, where particles of the extraction polarity are depleted due to ion evaporation.

2.1.3 Starting Voltage

A Taylor cone will develop once the electrostatic traction forces overcome the surface tension of the liquid. In this section, we follow the procedure given in reference [20] to find the required voltage applied to a liquid for it to sustain a Taylor cone. It is possible to find the starting voltage by solving for the electric field around an emitter and then matching the electrostatic pressure to the surface tension force, which is the

equilibrium condition under which the cone can be sustained. However, instead of solving for the field in the cone coordinate system as we did in section 2.1.1, we use a more convenient coordinate system that can take into account the overall shape of the emitter.

The prolate-spheroidal coordinate system is an orthogonal system with coordinates (η, ξ, ϕ). In terms of cartesian coordinates, the transformation is

$$\eta = \frac{r_1 - r_2}{a} \qquad \xi = \frac{r_1 + r_2}{a} \tag{2.20}$$

where

$$r_1 = \sqrt{x^2 + y^2 + \left(z + \frac{a}{2}\right)^2} \qquad r_2 = \sqrt{x^2 + y^2 + \left(z - \frac{a}{2}\right)^2} \tag{2.21}$$

Here, a is a scaling factor dependent on the overall size of the system, and ϕ is the angle about the z-axis. In this coordinate system, the lines of constant η are confocal hyperboloids while the lines of constant ξ are confocal ellipsoids with the same foci. We can take our emitter, which is a sharpened tip (with radius of curvature R_c) covered with liquid, to be approximately represented by a constant $\eta = \eta_0$ line, as shown in Fig. 2-4. The extractor can be represented by the $\eta = 0$ plane, placed a distance d away from the tip.

Before proceeding, we must find the relation between the tip-extractor distance d and the emitter radius of curvature R_c with the unknown scale factor a and unknown η_0. Along a constant η line, if $R^2 = x^2 + y^2$, the z-coordinate can be expressed as

$$z = \eta\sqrt{\frac{a^2}{4} + \frac{R^2}{1 - \eta^2}} \tag{2.22}$$

Thus, at the tip, where $R = 0$, $d = a\,\eta_0/2$. Furthermore, the radius of curvature ρ of the constant η surface is given by

$$\rho = \frac{1 - \eta^2}{2\eta} a \left(1 + 4\frac{R^2/a^2}{(1 - \eta^2)^2}\right) \tag{2.23}$$

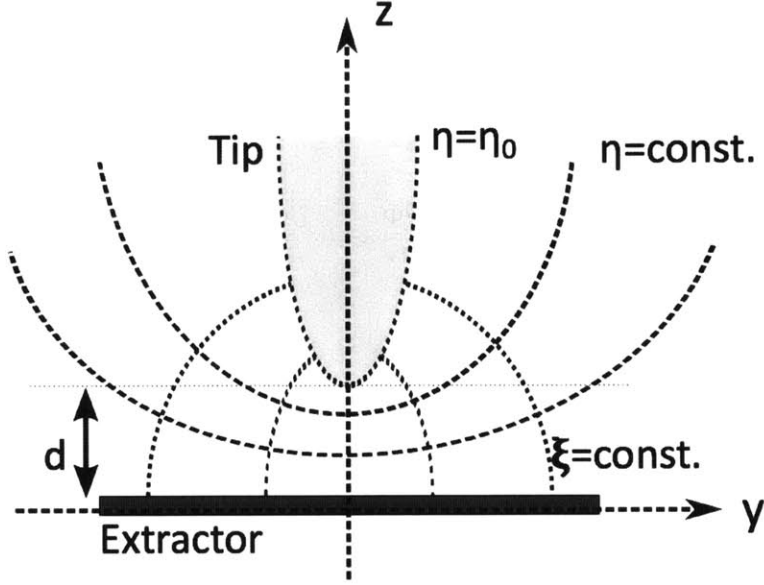

Figure 2-4: Prolate spheroidal coordinate system ($x = 0$ plane)

Evaluating at the tip apex,

$$\rho = R_c = \frac{1-\eta_0^2}{2\eta_0}\frac{2d}{\eta_0} \tag{2.24}$$

Thus, we find

$$\eta_0 = \left(1+\frac{R_c}{d}\right)^{-1/2} \qquad a = 2d\sqrt{1+\frac{R_c}{d}} \tag{2.25}$$

To find the electric field at the tip and the region surrounding the emitter, we solve Laplace's Equation for the potential, $\nabla^2\Phi = 0$, and impose boundary conditions. The potential should be $\Phi = V_0$ on the emitter surface ($\eta = \eta_0$) and $\Phi = 0$ on the extractor ($\eta = 0$). Because of the boundary conditions, the potential can depend only on the η coordinate, and so Laplace's equation reduces to

$$\frac{\partial}{\partial\eta}\left((1-\eta^2)\frac{\partial\Phi}{\partial\eta}\right) = 0 \tag{2.26}$$

The solution to equation 2.26 is

$$\Phi = V_0\frac{\tanh^{-1}\eta}{\tanh^{-1}\eta_0} \tag{2.27}$$

And from here, we can calculate the electric field at the point $(x = 0, y = 0, z = d)$ and hence the electrostatic pressure at the apex of the emitter. The electric field at the apex of the emitter is given by

$$E_{tip} = -\frac{\partial \Phi}{\partial z} = -\frac{\partial \Phi}{\partial \eta}\frac{\partial \eta}{\partial z} \tag{2.28}$$

If we assume $R_c \ll d$ (which is often the case, as for ILIS, R_c is about 10 μm and d is roughly a mm), the electric field at the tip reduces to

$$E_{tip} = -\frac{2V_0/R_c}{\ln\left(4d/R_c\right)} \tag{2.29}$$

For the Taylor cone to exist, the equilibrium condition requires the electrostatic pressure at tip to match the surface tension, i.e.,

$$\frac{1}{2}\epsilon_0 E_{tip}^2 = \frac{2\gamma}{R_c} \tag{2.30}$$

and finally, by substituting 2.29 in 2.30, we find an expression for the start voltage:

$$V_{start} = \sqrt{\frac{\gamma R_c}{\epsilon_0}} \ln\left(\frac{4d}{R_c}\right) \tag{2.31}$$

We note there is a weak dependence on the tip-extractor distance for the start-up voltage of an ILIS, but the key factors determining this onset are the surface tension of the liquid and the tip radius of curvature. For instance, for an ILIS wetted with the ionic liquid EMI-BF_4, with $R_c \sim 10$ μm, and $d = 1$ mm, $V_{start} = 1350$ V. This value is of the same order as experimental values reported [17]. It has been verified that the start-up voltage increases as a function of tip radius [2], and we observe such dependencies in some of the experimental results presented in this thesis.

2.2 ILIS performance in FIB

2.2.1 Brightness and Energy Characteristics of ILIS Beams

As discussed in Chapter 1, an ion source's brightness and energy spread are key parameters in determining how well the beam can be focused.

We estimate the brightness than can be obtained from an ILIS by considering the size of the emission site. An ILIS can operate at a current of 600 nA, and the beam angular spread has been measured experimentally to be about 18° [17]. If we take the size of the emission site to be $D = 20$ nm, we find a value of $\beta = 6.16 \cdot 10^5$ Acm^{-2}sr^{-1}. This value is on the order of the quoted requirement, and could be improved by operating ILIS at higher currents (by increasing the operation temperature or using liquids of higher conductivity).

For FIB, it is of utmost importance to minimize the energy spread of an ion beam in order to limit the contributions of lens chromatic aberrations to the probe size. ILIS beams contain ion populations with energy characteristics that make them adequate for FIB; Lozano measured the energy profiles of several ionic liquids using Retarding Potential Analyzer (RPA) techniques. The author measured the beam after focusing it through an Einzel lens, used for guiding the beam into the detector. The use of the lens could filter out some of the particles coming at energies different from the main energy peak. Nonetheless, it was determined that a the majority of the beam has energy spreads of 6-8 eV for the liquids EMI-Im [1] and EMI-BF_4, with energy deficits of 6-7 eV[19, 16]. The deficit can be attributed to the energy required for ion evaporation, whereas the energy spread can be attributed to possible variations in the electric field along the finite emission site. This energy distributions are very promising for FIB, although we must take into account the energy distribution of the whole beam.

An ionic liquid composed of anions (A-) and cations (C+) will produce ion species $(AC)_n$A- or $(AC)_n$C+, for the negative and positive extraction polarity, respectively, and where n, the degree of solvation, is the number of neutral clusters attached to the

[1] 1-ethyl-3-methylimidazolium bis(triflouromethylsulfonyl)amide

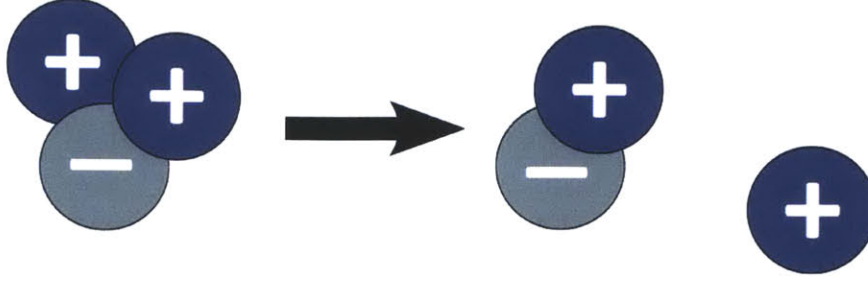

Figure 2-5: Diagram of break-up from n=1 to n=0

ion (n =0, 1 and sometimes 2). For example, previous time-of-flight spectrometry for the liquid EMI-BF_4 indicates that the current in the beam is roughly equally divided between the n=0 and n=1 degrees of solvation [17], with some minor contribution of larger species. It was found that the heaviest species ($n \geq 1$) are metastable, and they can break during flight, yielding neutrals and a new ion. (see Fig. 2-5). From experimental observations, it is known that breakup can happen in regions of zero potential as well as in the acceleration zone between the emitter and the extractor [19, 6, 5]. For FIB applications, these neutrals could lead to undesired effects in the sample as they are not manipulated by optics. Furthermore, the break-up significantly affects the energy distribution of the beam, as we explain in this section. A concern of this thesis is determining the distribution of neutral particles within the beam.

A large fraction of the current in the beam corresponds to a monoenergetic population with an energy close to the applied potential, but there is also a population of ions coming with a continuum of energies below the main energy peak, since these ions are the result of breakup of larger species [19]. Ideally, all ions should have a final kinetic energy $K = qV_{app}$, where V_{app} is the applied potential. However, if an ion with degree of solvation n and mass m_n breaks into a neutral and ion with degree of solvation m ($m < n$) and mass m_m, at a region with potential V_b (say, in between the emitter and the extractor, where the potential varies from V_{app} to ground), then the final kinetic energy of the ion resulting from breakup will be

$$K_m = qV_b + \frac{m_m}{m_n} q \mid V_{app-} V_b \mid . \tag{2.32}$$

If ions break up in the acceleration zone, their energies can range between $m_m q V_{app}/m_n$ (if break-up occurs after the heavy ion is fully accelerated) and up to qV_{app} (if fragmentation occurs immediately after emission, $V_b = V_{app}$). The ions resulting from break-up are therefore not suitable for FIB, as their energy distribution is wide and will lead to chromatic aberrations in the beam. In order to implement ILIS in FIB, it would be necessary to select only the monoenergetic population of ions in the beam, eliminating neutrals and ion fragments. FIB performance could also be further improved by selecting one ionic species within the ion beam. It is likely that different degrees of solvation could have different, although close, beam energies, since they could have different energy barriers for ion evaporation [37]. Then, it is likely that the energy spread could be less than the 6-8 eV quoted so far by choosing only the monoenergetic monomers in the beam for focusing.

2.2.2 Probe Size Estimation and Preliminary Focusing

The probe size for an ILIS can be estimated[2], using the expression we introduced in chapter 1:

$$d^2 = \frac{I^3}{4}\frac{C_s^2}{[\pi M^2 \frac{dI}{d\Omega}]^3} + I\left(\frac{\Delta W_{1/2}}{W}\right)^2 \frac{C_c^2}{[\pi M^2 \frac{dI}{d\Omega}]} + M^2 D^2 \tag{2.33}$$

We take aberration coefficients of $C_s = 1000$ mm and $C_c = 10$ mm, and take a magnification $M = 1$. The analysis is for an ILIS operating with a current of 600 nA, with a beam half-angle of 18° [17]. If we assume the current spread to be constant, the current angular spread is $\frac{dI}{d\Omega} = 1.95$ μAsr^{-1}. The energy spread is assumed to be 7 eV with a beam energy of 3 keV. The source size is taken to be $D = 20$ nm. We recall that I is the current accepted into the optical system through a small aperture, and might not be equal to the current emitted by the source.

The contributions from the source size magnification and the spherical and chro-

[2] This estimation was performed in reference [37]. It is performed here again for the sake of completeness; this estimation uses different constants, in particular the source size is taken to be 20 nm instead of 10.

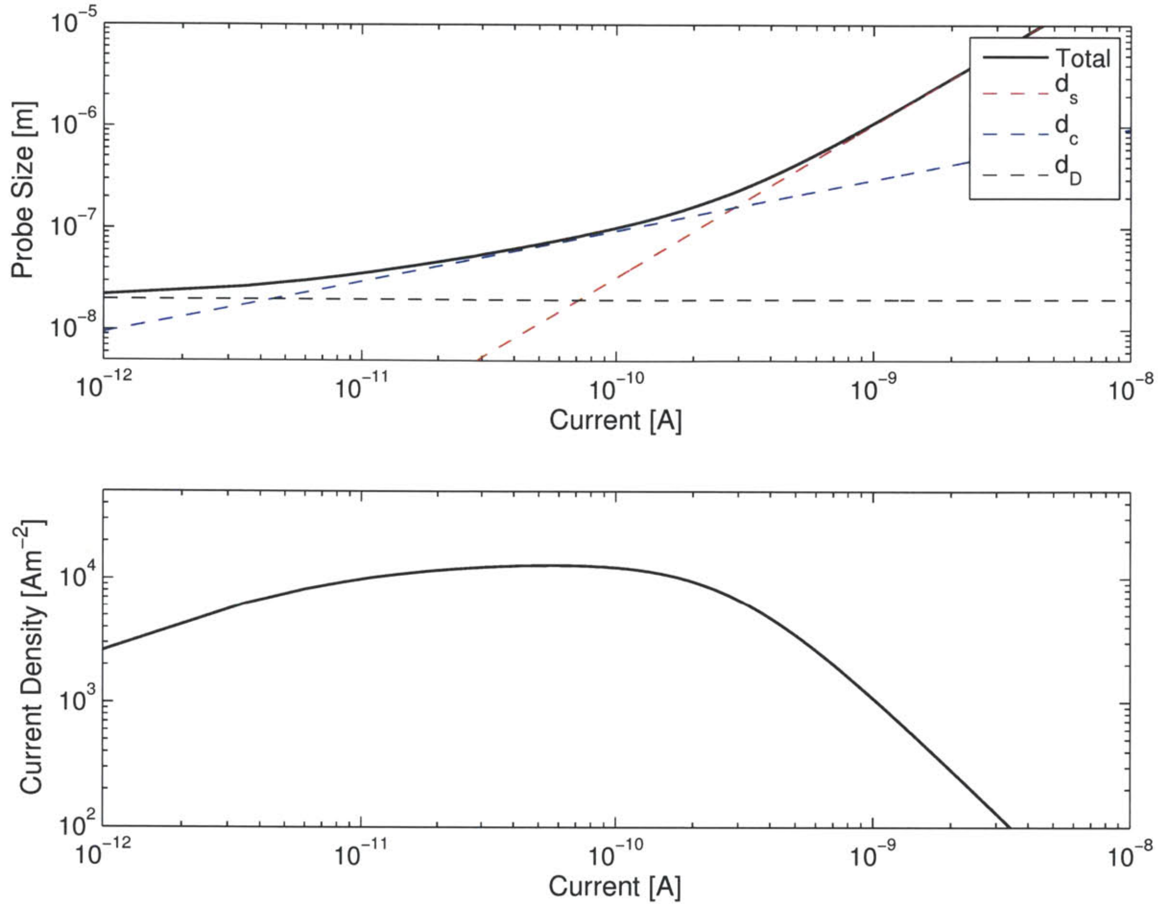

Figure 2-6: Probe Size and Probe Current Density for a hypothetical ILIS FIB

matic aberrations to the total probe size are illustrated in Fig. 2-6. We also plot the current density of the probe, which is equal to $J_{probe} = \frac{4I}{\pi d^2}$. From the probe size plot, it is clear that at high currents, the spherical contribution dominates the probe size, whereas if the current is reduced to pA levels, the aberrations stop contributing and the probe size is effectively equal to the source size magnification. At intermediate current levels, where the current density is the highest, the current is dominated by chromatic aberrations. Table 2.1 shows some sample values. At a current of 10 pA, it could be possible to achieve a 36 nm probe size with a current density of almost 1 Acm^{-2}. For comparison, a Ga LMIS can produce 30 nm probes at 50 pA currents [30], which give current densities of 7 Acm^2.

The values here are provided as an estimate and can vary depending on the optical properties of the lens. Also, our estimation only takes into account one lens,

I [nA]	d [μm]	J_{probe} [Acm^{-2}]
1	1	1.08
0.1	0.1	1.23
0.05	0.071	1.27
0.01	.036	0.985

Table 2.1: Probe sizes and current densities

although, in practice, FIB columns use two lenses, one for initial focusing and another just above the sample, for focusing after the beam has been deflected. Therefore, better resolutions could be expected if using two lenses. Another observation is that we have used a magnification of 1; it is possible to reduce the probe size by using smaller magnifications (although $M < 0.1$ is not practical with two lens systems [22]). There is a trade-off at smaller magnifications as the contributions from chromatic and spherical aberrations increase, but an optimum magnification can be found. The chromatic aberration is also a function of the beam energy, and can be significantly lessened by using higher acceleration voltages for the beam. The energy spread of 7 eV could be reduced if only one ion species were to be selected.

The hypothetical performance of ILIS as a source for FIB is encouraging; as a proof-of-concept, Zorzos and Lozano built a simple column with a single Einzel Lens with an ILIS operating with the ionic liquid EMI-BF_4 [37]. An aperture was used to limit the current accepted into the lens to 0.7 nA. The authors achieved a minimum probe size of 30 μm; however, it must be noted that the optical parameters of the lens were not known, and that the beam accepted into the lens contained multiple ion species and ions resulting from break-up. Although the less energetic ions are scattered away by the lens, it is likely that ions with energies different from the main energy peak were in the focused beam and this resulted in increased chromatic aberration.

2.3 Thesis Contributions

In this thesis, we do not explore further the focusing capabilities of ILIS, but rather aim to characterize basic properties such as the beam behavior under different conditions to determine the stable regimes of the ILIS. We report current-voltage measurements coupled with direct visualization of the beam, to determine the range of voltages over which emission is stable. In addition, we estimate the neutral particle fraction in the beam via retarding potential analysis, and use the visualization tool to determine the distribution of these neutral particles in the beam. This information should be useful for the optimization of ILIS for FIB implementation as well as in the design of optical systems and filtering equipment required for focusing.

Chapter 3

Experimental Techniques

In this chapter, we discuss the techniques for fabrication of the ionic liquid ion source specimens used for characterization, as well as the visualization system and the retarding potential analyzer setups used for energy characterization.

3.1 Source Fabrication and Emitter-Extractor Setup

The emitters used in the experiments reported in this thesis are externally wetted tungsten needles. The emitter fabrication has two main steps: (1) sharpening of the wire to obtain a tip diameter of ~ 5 µm, and (2) micro roughening, which creates grooves along the emitter surface that facilitate liquid flow. The fabrication process is similar to the one presented in reference [17], although we skip the emitter annealing step.

The starting material for the emitter is a straight, 0.5 mm diameter Goodfellow 99.9% purity tungsten wire. The wire is cut using a rotating saw into approximately 28 mm long pieces. Before sharpening, the wire pieces are cleaned in an ultrasonic bath, first in isopropanol and then in acetone.

The wire is sharpened by electrochemical etching in a NaOH (1 N) solution. The cathode for the reaction is a 3.81 cm diameter stainless steel cylinder, and the anode is the tungsten wire, placed concentrically in the cylinder, as shown in Fig. 3-1. The sharpening process requires three steps:

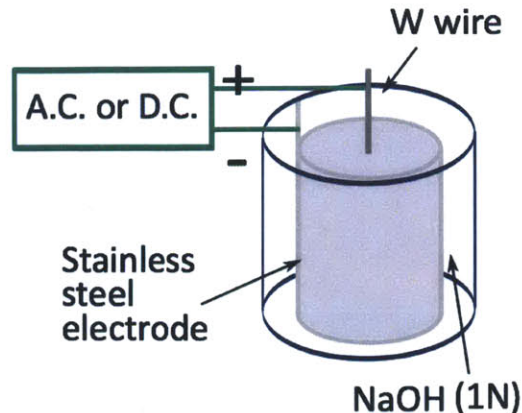

Figure 3-1: Electrochemical Etching Setup

1. In order to remove the native oxide layer on the surface of the tungsten, the wire is dipped as much as possible into the NaOH solution, and a 10 V (peak to peak) A.C. signal (60 Hz) is applied during 10 seconds between the tip and the cylinder. The signal is produced by an Agilent 33220A signal generator amplified by a KEPCO 36-12D bipolar power supply.

2. A sharp end is achieved by submerging the wire 3 mm into the solution, and applying 50 V D.C. between the tip and the cylinder until the wire in the solution dissolves. A TENMA 72-6615 DC power supply is used for this step.

3. The emitter is shaped so that it has a smooth transition between the shank and the tip. For this step, a 20 V (peak to peak) 60 Hz sinusoidal signal is applied during 30 seconds, using the same power supply setup used in step 1.

The emitter is then cleaned in deionized water and acetone in the ultrasonic bath. Then, to improve wettability of the emitter by the ionic liquid, the surface of the emitter is micro roughed in a hot solution of NaOH (1 N) and $K_3Fe(CN)_6$. To prepare this solution, approximately 25 ml of NaOH are heated until the liquid reaches 98°C. Then, several grams of $K_3Fe(CN)_6$ are added slowly, while stirring, until the solution becomes saturated. The stirring is turned off and the clean emitter is submerged for 40 seconds in the hot bath. The needle is then immediately cleaned, first in deionized water and then in acetone, and blow-dried with nitrogen. After this treatment, the emitter will have small grooves along its surface that allow the liquid to flow towards

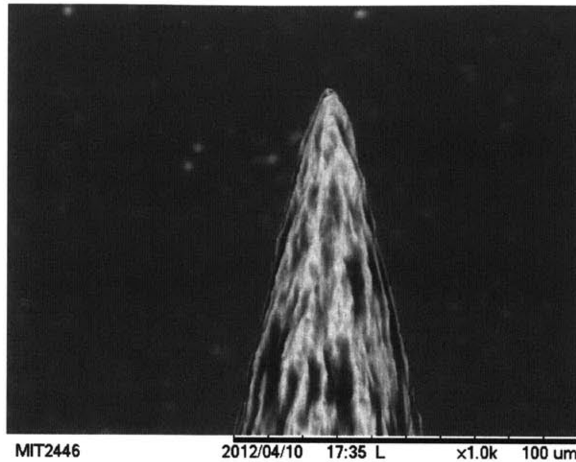

Figure 3-2: Scanning electron micrograph of ILIS tip after wetting with EMI-BF_4.

the apex. The needle is wet at ambient conditions by applying a small drop of liquid to the emitter with a syringe, and the resulting emitter is inspected in a scanning electron microscope. A sample emitter is shown in Fig. 3-2.

The emitter is held in place by a copper clamp; the copper piece contains a 2.54 mm diameter stainless steel cylinder filled with ionic liquid, which serves as a liquid reservoir, located approximately 3 mm away from the emitter apex. The voltage is applied to the emitter through the copper clamp. The extractor consists of a grounded stainless steel plate with a 1.6 mm diameter aperture. For some of the visualization experiments reported in this thesis, the extractor is followed by another grounded stainless steel plate with a 4.76 mm diameter aperture. This second plate functions as a shield, and holds a small magnet (placed 1 cm off the beam axis), which traps any secondary electrons produced if ions impact components of the experimental setup or the chamber walls. These secondary electrons should be suppressed as they might provoke undesired signals on the visualization experiments here reported.

A signal generator (Agilent 33220A) connected to a bipolar high-voltage power supply (Matusada AMS-5B6) is used to direct the voltage applied to the tip. The current emitted by the source is determined by measuring the voltage drop across a 1 MΩ resistor placed in series with the power supply. For all experiments reported in this thesis, the ILIS emission is conducted at room temperature at pressures below 10^{-6} Torr.

3.2 Ion Beam Visualization

The ILIS copper clamp is placed on a triaxial stage with sub micron resolution (Physik Instrumente model M-112), while the extractor is held fixed. In this way, we can adjust the emitter position with respect to the extractor *in situ*. The stage and extractor are placed in a vacuum chamber, so that the beam is directed toward a beam visualization system (BVS) located at the side of the chamber. A diagram of the visualization system and vacuum chamber pictures are shown in Fig. 3-3.

The extractor is placed several centimeters away from the entrance of the BVS, which is composed of a set of nickel attenuating grids (1% transparency), a microchannel plate (MCP) detector and a phosphor screen. The nickel grids are spaced 12.7 mm away from each other, and the MCP is located immediately behind the last nickel grid. The MCP and phosphor screen are separated by a 1.5 mm thick ceramic spacer. When a sufficiently energetic particle, such as an ion or a neutral, hits the surface of one of the channels in the plate, electrons will be emitted from the surface and be driven toward the back of the microchannel plate by the applied potential V_{MCP}. The electrons then hit the phosphor screen, which is biased at a positive potential V_P to further accelerate them. The phosphor screen will glow when impacted by electrons and the image is recorded with a CCD camera. The imaging area is 44 mm in diameter and the two high-voltage power supplies used for the MCP and phosphor screen are Bertan Series 230.

It should be emphasized that this visualization tool serves only to determine basic trajectory information of the beam and the profiles obtained might not contain the full information of the beam size. The size and intensity of the spots captured by the viewing system depends on V_{MCP} and V_P, as well as on the aperture used for the camera. For instance, for a fixed V_P, it is possible to obtain a wider and more intense spot in the viewing system by increasing V_{MCP}, i.e, the larger bias, the better the detection of the particles in the beam by the MCP. Furthermore, the camera might not be able to capture completely the light produced by the phosphor screen, and the recorded profile represents only a fraction of the actual spectra produced by the

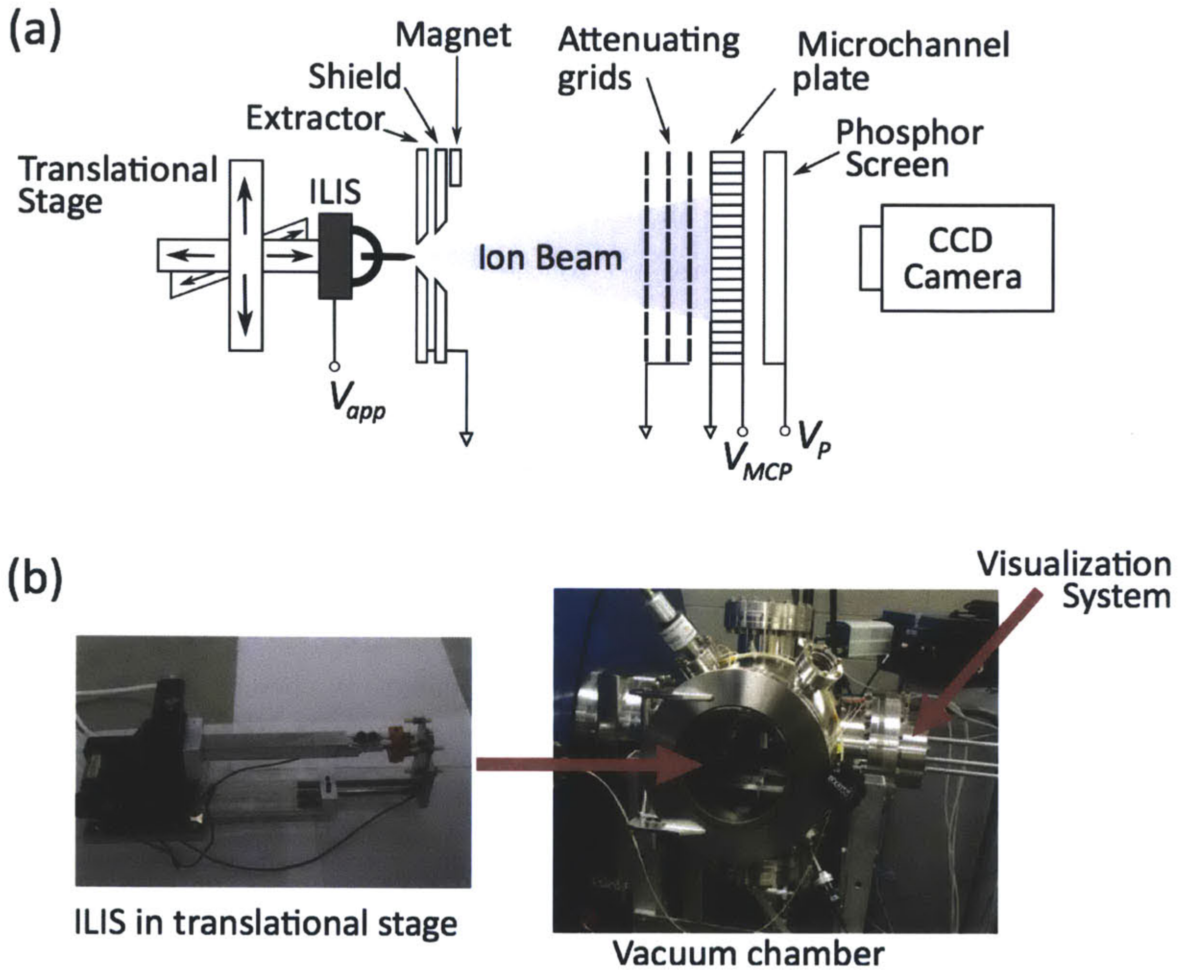

Figure 3-3: (a) Visualization setup diagram (b) Pictures of experimental setup

phosphor. Another artifact posed by this system is that, at high V_{MCP} or V_P, the light produced by the phosphor is more intense than can be captured by the camera, and thus the images appear saturated. The measurements presented in this thesis are therefore a qualitative description of the beam profiles, as they do not capture the full beam behavior; nevertheless, they provide the spatial distribution information required to complement electrical measurements and determine the basic trajectories of the beam.

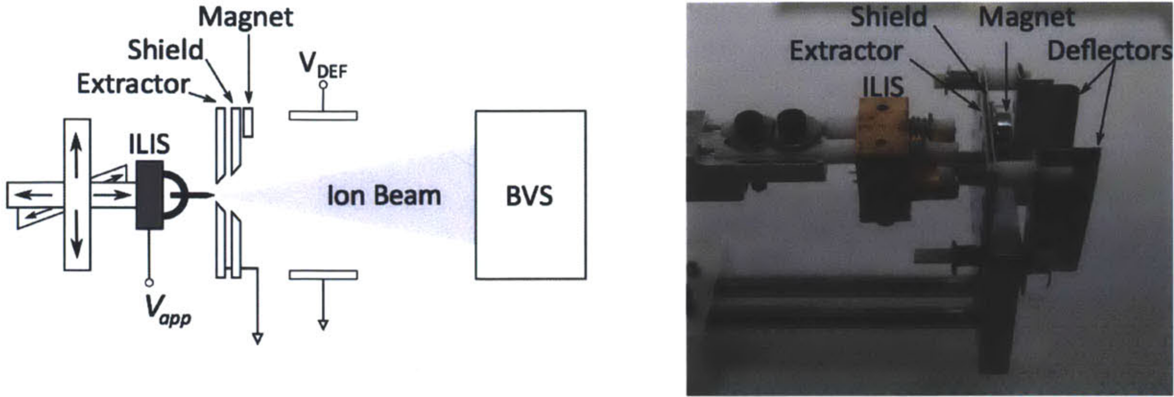

Figure 3-4: Visualization setup with deflector plates

3.3 Neutral Beam Visualization

The neutral beam visualization setup is very similar to the beam visualization setup described before. In order to visualize only the neutral population within the beam, we have installed two stainless steel deflector plates 7 mm downstream from the extractor exit. A diagram and picture of the setup with the deflectors is shown in Fig. 3-4.

The plates are 12.7 mm wide (in the direction of the beam axis) and are separated from each other by 20 mm. One of the plates is biased to a potential V_{DEF}, while the other plate is kept grounded. The deflector plates produce a roughly uniform electric field along the path of the beam, and thus deviate the charged particles from their normal trajectory, but do not affect the neutral particle trajectory. Two sample ion trajectories are plotted on Fig. 3-5 for different deflection voltages; we note that the MCP entrance is located about 7 cm away from the deflector entrance, and so the ions that entered the deflector should have been deflected by 25 mm as they enter the MCP. Therefore, the signal measured at the center of the imaging area should correspond to neutral particles only.

For these neutral visualization tests, we apply a square wave signal to the emitter from $-V_{app}$ to V_{app} with a period of 10 s. A 1-2 kV voltage is applied to the biased plate of the deflector every other period of the emitter, in such a way that we can image the full beam in both polarities over one period and the neutral particles in

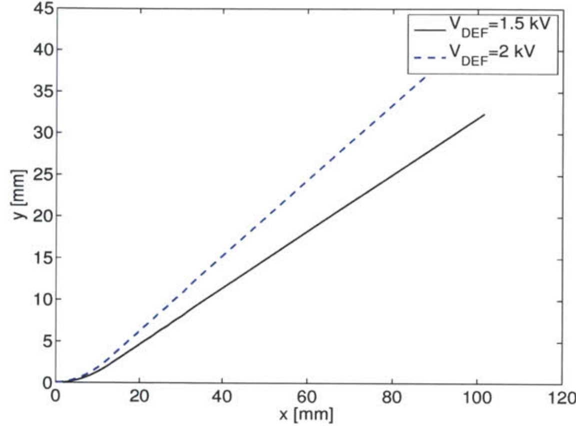

Figure 3-5: Sample trajectories of EMI$^+$ for different deflection voltages. The entrance of the deflector is at x=0.

both polarities over the next period. The voltage of the deflector plate is controlled in a similar fashion to the voltage applied to the needle, using an Agilent 33220A signal generator to direct a Matsusada AMS-5B6 power supply.

3.4 Retarding Potential Analysis

In order to estimate the percentage of the beam current that results from ion breakup for the operating conditions used for the visualization experiments, we fire the ILIS beam toward a retarding potential analyzer (RPA). The RPA is composed of five grids, followed by a Faraday cup detector. A diagram of the RPA is shown in Fig. 3-6. All grids are 90 % transparent tungsten mesh. The entrance grid is grounded and located 26 mm downstream of the extractor. The next three grids serve as the retarding grids, and are followed by a secondary electron retarding grid, biased to -15 V. The Faraday cup functions as a collector, and is connected to an oscilloscope (Agilent DSO-X 3024A) through a high impedance electrometer (Keithley 6514).

If the bias V_{RP} applied to the retarding grids exceeds the energy of a particle in the beam, that particle then cannot reach the collector. Therefore, if we apply different V_{RP} to the retarding grids, we can sample the amount of particles that are present in the beam at a given energy and obtain a profile of the energy distribution. In the experiments reported here, a high-voltage triangular wave is applied to the retarding

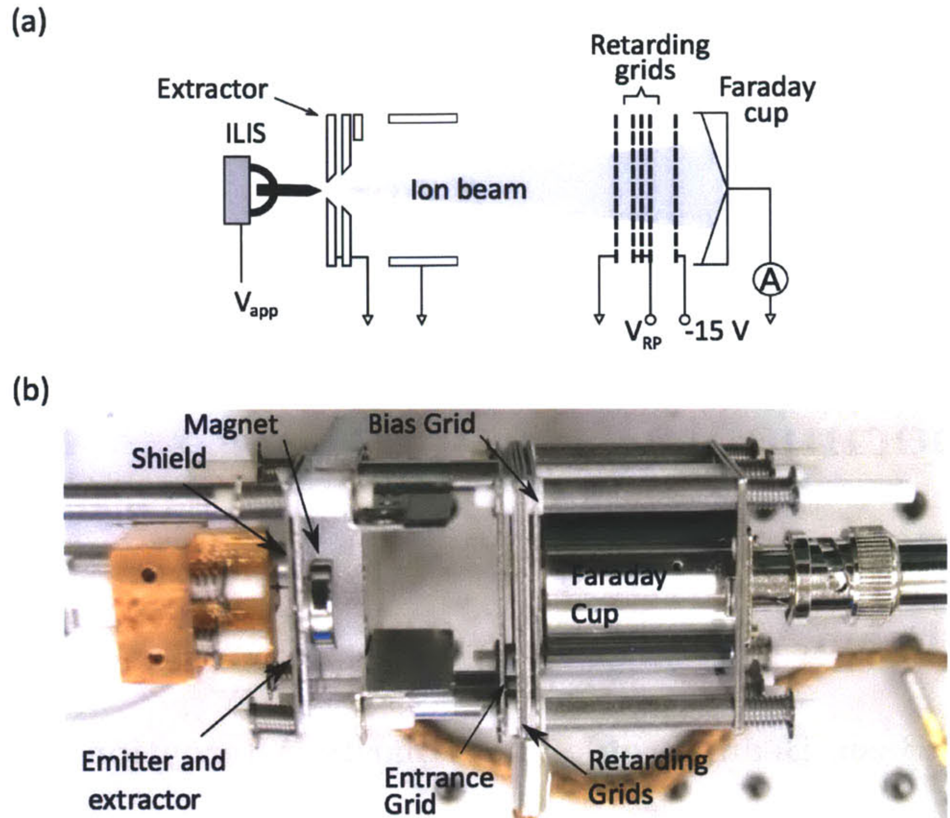

Figure 3-6: (a) RPA diagram (b) Picture of setup

grids while the ILIS is emitting, and the collected current signal is processed using a low pass filter to remove noise.

Chapter 4

Experimental Results

4.1 Beam Visualization

4.1.1 Basic Beam Profile and Polarity Alternation Stability

We use the visualization system to determine the basic beam profile and the behavior of the beam as the applied voltage is switched between the negative and positive polarities.[1] The tests reported in this section were performed with an emitter fabricated using a process slightly different from the one described in section 3.1. This tip is held in place by a tungsten loop that functions as a liquid reservoir rather than by a copper clamp. The tip is sharpened and microroughed in a similar fashion to that described in section 3.1, but with an additional preparation step. The tip-loop assembly is annealed in vacuum for six minutes using a current of 4.69 A, and the emitter is wetted in vacuum after it has cooled. The purpose of this step is to reconstruct the metal grain boundaries into longitudinal grooves to facilitate the liquid flow, as well as to provide a clean surface for liquid application. This additional step is not required for emission to occur, and we do not perform it for any of the other tests reported in this thesis.

For the polarity alternation test, the emitter-extractor assembly is placed in the chamber with the visualization system; the distance between the extractor and the

[1]Most of the results presented in this chapter were reported in references [25] and [27]

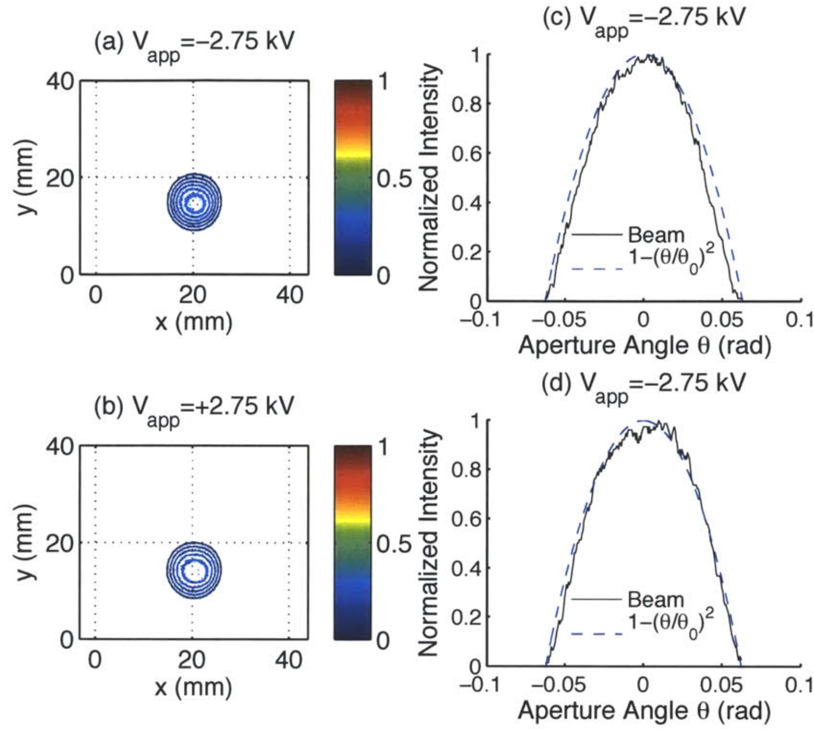

Figure 4-1: Beam profiles for emission in alternating polarity. (a and b) Contour plots of beam profile in negative and positive mode, respectively. (c and d) Beam profile cross-section in negative and positive mode, respectively, with comparison to theoretical parabolic distribution.

MCP entrance is set to approximately 10 cm. The visualization system has three attenuation grids, and we set V_{MCP} and V_P to 0.73 kV and 4 kV, respectively. The emitter is placed 0.3 mm away from the extractor using the positioning stage, and then the ILIS is tested in alternating polarity, with $V_{app} = \pm 2.75$ kV over a period of 5 s, while recording the spectra from the viewing system. The current changes from 190 nA in the positive polarity to 105 nA in the negative polarity.

A contour plot of the negative and positive modes beam profiles can be observed in Fig. 4-1 (a) and (b). All visualization data obtained in this thesis is plotted as a function of the imaging area, with x and y the spatial coordinates of the image captured. We also normalize the signal strength of all captured profiles to the maximum pixel intensity captured by the visualization system. In Fig. 4-1, each image is the average of five frames taken every 0.5 s, in order to reduce noise.

The contour plots of Fig. 4-1 show that the beam direction does not change position with the change of polarity. Furthermore, we can use this data to estimate the profile of the beam; as noted before, the visualization system might not capture the edges of the distribution, but we can still extract a basic beam profile. Indirect evidence in previous research [16, 17] suggests a parabolic profile distribution for ILIS beams, of the form

$$f(\theta) = \frac{3}{2\theta_0}\left(1 - \left(\frac{\theta}{\theta_0}\right)^2\right) \tag{4.1}$$

which integrates to unity in $[0, \theta_0]$ and where θ_0 represents the beam half angle. For both polarities, Figs. 4-1(c) and (d) show that the beam profile (normalized to the maximum intensity of the impact) is close to the parabolic estimate.

4.1.2 Influence of the Applied Voltage

We use the visualization system to determine the change in behavior of the beam as the applied voltage is increased in both polarities. We use an emitter fabricated with the procedure described in section 3.1, and wetted with the liquid EMI-BF_4.

For these tests, the distance between the extractor and the MCP is set to 7.7 cm. Due to the wear of the MCP from ion beam irradiation, only one attenuating grid is used for these experiments, in order to increase the signals obtained in the viewing system. We perform several experiments, increasing the applied voltage gradually while recording the emitted current and beam profile. All of the images presented in this section correspond to single snapshots of the visualization area.

We perform a first voltage variation experiment with the emitter placed 0.6 mm behind the extractor plane. In this position, the starting voltage for emission is about ±1.1 kV. Fig. 4-2 shows the impacts of the beam in 100 V increments for applied voltages from $V_{app} = 1.1$ kV to $V_{app} = 1.7$ kV, and Fig. 4-3 shows the impacts of the beam in -100 V increments from $V_{app} = -1.1$ kV and $V_{app} = -1.5$ kV. The currents emitted from the source at each condition are shown in the figures. The biases of the visualization system for the two sweeps are $V_{MCP} = 1.8$ kV and $V_P = 5$ kV.

At voltages close to the starting potential, the source has a single emission site as

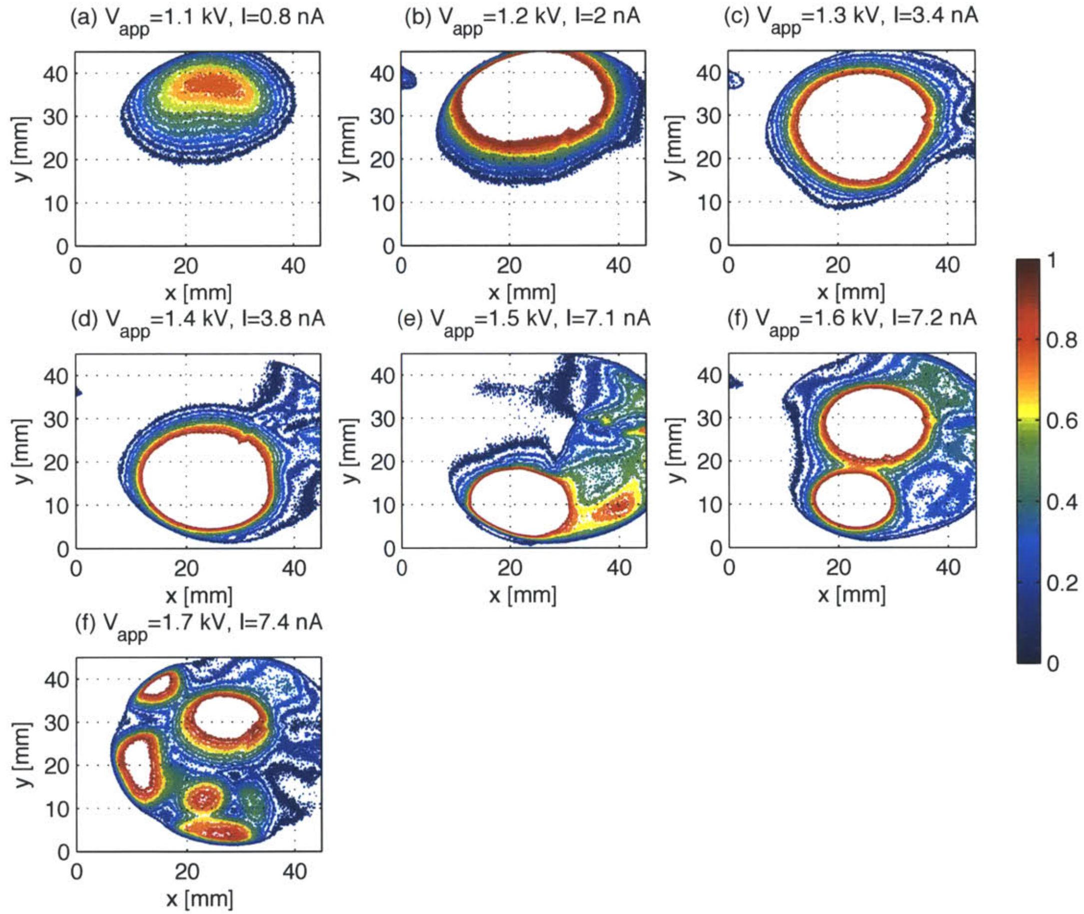

Figure 4-2: (a)-(f) Beam profiles for emitter voltages from $V_{app} = 1.1$ to $V_{app} = 1.7\,\mathrm{kV}$. We note that the profiles appear rounded off as the BVS has a circular imaging area; data appearing near $x = 0$ mm, $y = 40$ mm corresponds to reflections of light on the metal surrounding the imaging area.

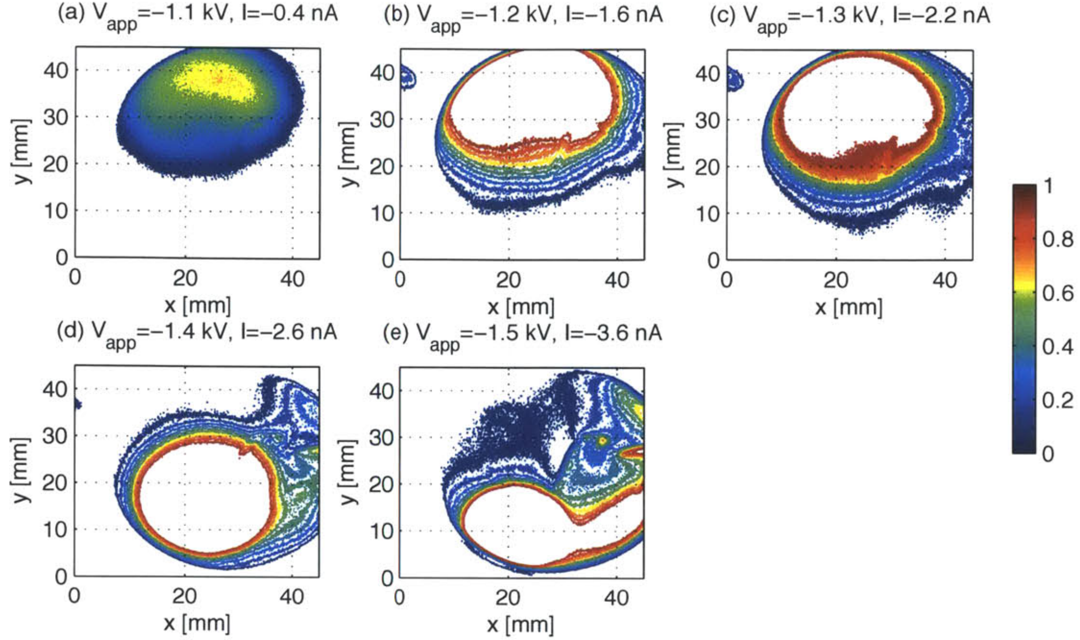

Figure 4-3: (a)-(f) Beam profiles for emitter voltages from $V_{app} = -1.1$ kV to $V_{app} = -1.6$ kV.

shown by the single impact in the viewing area in Fig. 4-2 (a)-(d) and Fig.4-3 (a)-(d). The beam profile appears distorted, but this is due to known imperfections in the MCP. Also, as the potential is increased, the current emitted and the intensity of the profile also increase, and the viewing system becomes saturated (i.e., the maximum intensity sensed by the camera is recorded instead of the actual intensity). Therefore, it is not possible to distinguish the shape of the beam in the center of the impacts at higher extraction voltages, although it is expected from the measurements performed at higher currents (e.g. section 4.1.1) that the shape should remain parabolic. As the applied voltage is further increased, it can be seen that the source transitions from single to multiple beam emission, as revealed by the multiple impacts in the viewing system (Fig. 4-2(e),(f),(g) and 4-3(e)). It is observed that this multiple beam regime is unstable, as the source might produce more beams or the beams might move in a random fashion.

A second voltage sweep is performed with the emitter placed as close as possible to the extractor plane. The starting voltage is reduced at this smaller distance to

the extractor, and emission is obtained at ± 1 kV. Fig. 4-4 shows the impacts of the beam in 50 V increments for applied voltages from $V_{app} = 1$ kV to $V_{app} = 1.5$ kV, and Fig. 4-5 shows the impacts of the beam in -50 V increments from $V_{app} = -1$ kV to $V_{app} = -1.5$ kV. The biases of the viewing system are $V_{MCP} = 1.5$ kV and $V_P = 4.3$ kV for this trial.

At the lower biases of the visualization system, the beam impacts of this trial appear smaller than those in Figs. 4-2 and 4-3, as the smaller flux of particles at the edges of the beam cannot be detected at the low gain settings. However, the same trends are observed. The source emits a single beam at voltages close to the startup potential, and multiple beam emission occurs as the operation voltage is increased.

The multiple beam behavior is also observed on a tip of slightly different geometry. This tip was fabricated using the same procedure specified in section 3.1, although the smoothing step was extended to one minute instead of 30 seconds; this results in a tip with a radius of curvature of ~ 15 μm, rather than the 5 μm obtained with the shorter etch time. The wider tip, as indicated by equation (2.31), should have a higher startup voltage, and we verify this experimentally. The starting voltage is 2 kV when the emitter is placed 0.3 mm behind the extractor. We increase the voltage from the startup voltage to 2.2 kV and to 2.4 kV, and record the beam impacts in the BVS (for this experiments, three attenuating grids were used, and we set $V_{MCP} = 1$ kV and $V_P = 4$ kV). The profiles are shown in Fig. 4-6; again, we observe that as the applied voltage is increased, the source sustains multiple beam emission.

Why does the source transition from single to multiple beam behavior? It is possible to explain the transition by considering the electric field at the emitter. At first, the applied voltage produces an electric field high enough to sustain emission only at the apex of the emitter, where the radius of curvature is the smallest; this is illustrated in Fig. 4-7(a). However, as the voltage is increased, the electric field is high enough at locations upstream from the apex, and it is possible to sustain multiple Taylor cones (Fig. 4-7(b)).

It should also be considered that the emitters used have rough surfaces that are required to enable liquid flow to the tip. The electric field must be normal to the

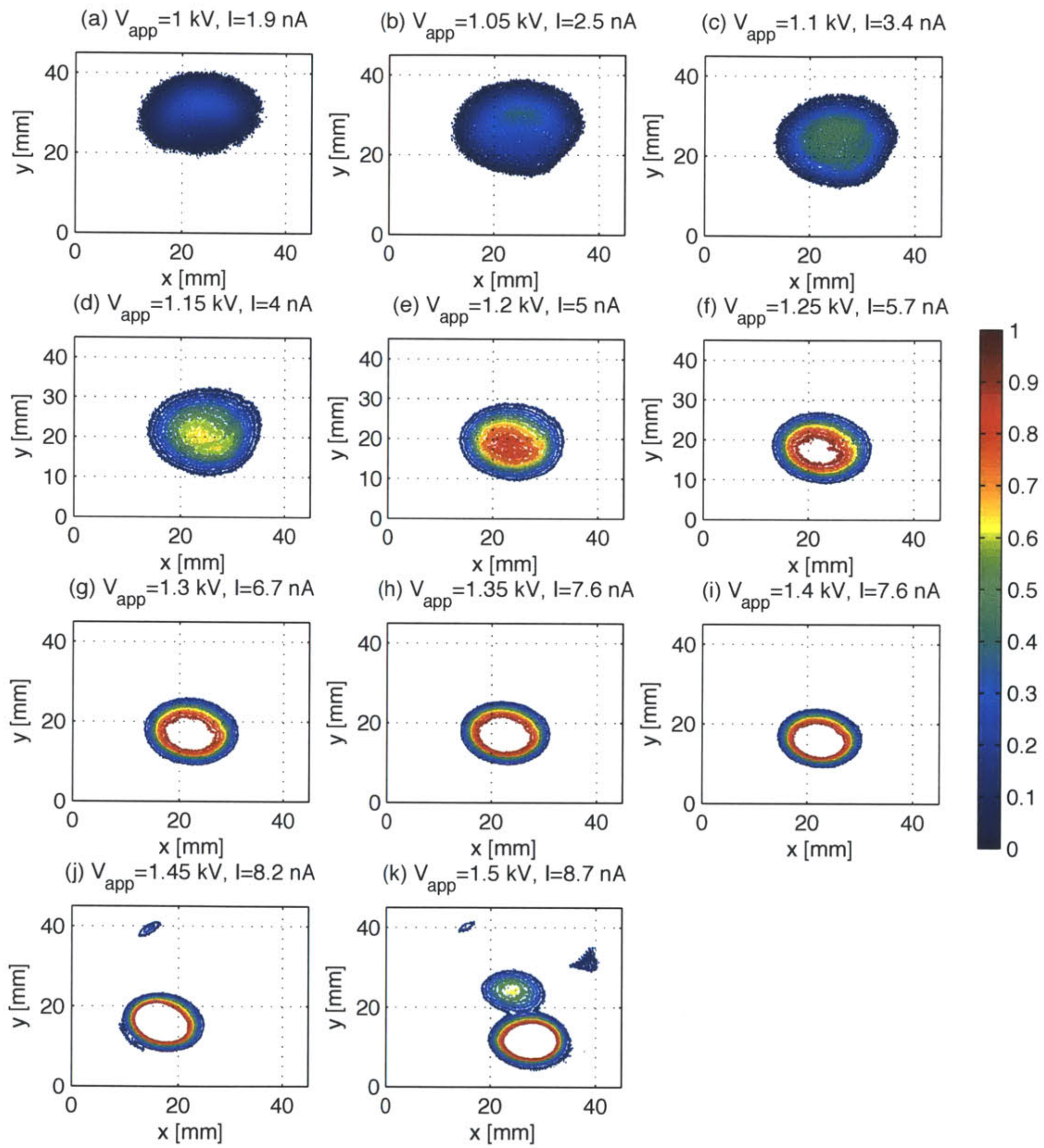

Figure 4-4: (a)-(k) Beam profiles for emitter voltages from $V_{app} = 1$ kV to $V_{app} = 1.5$ kV

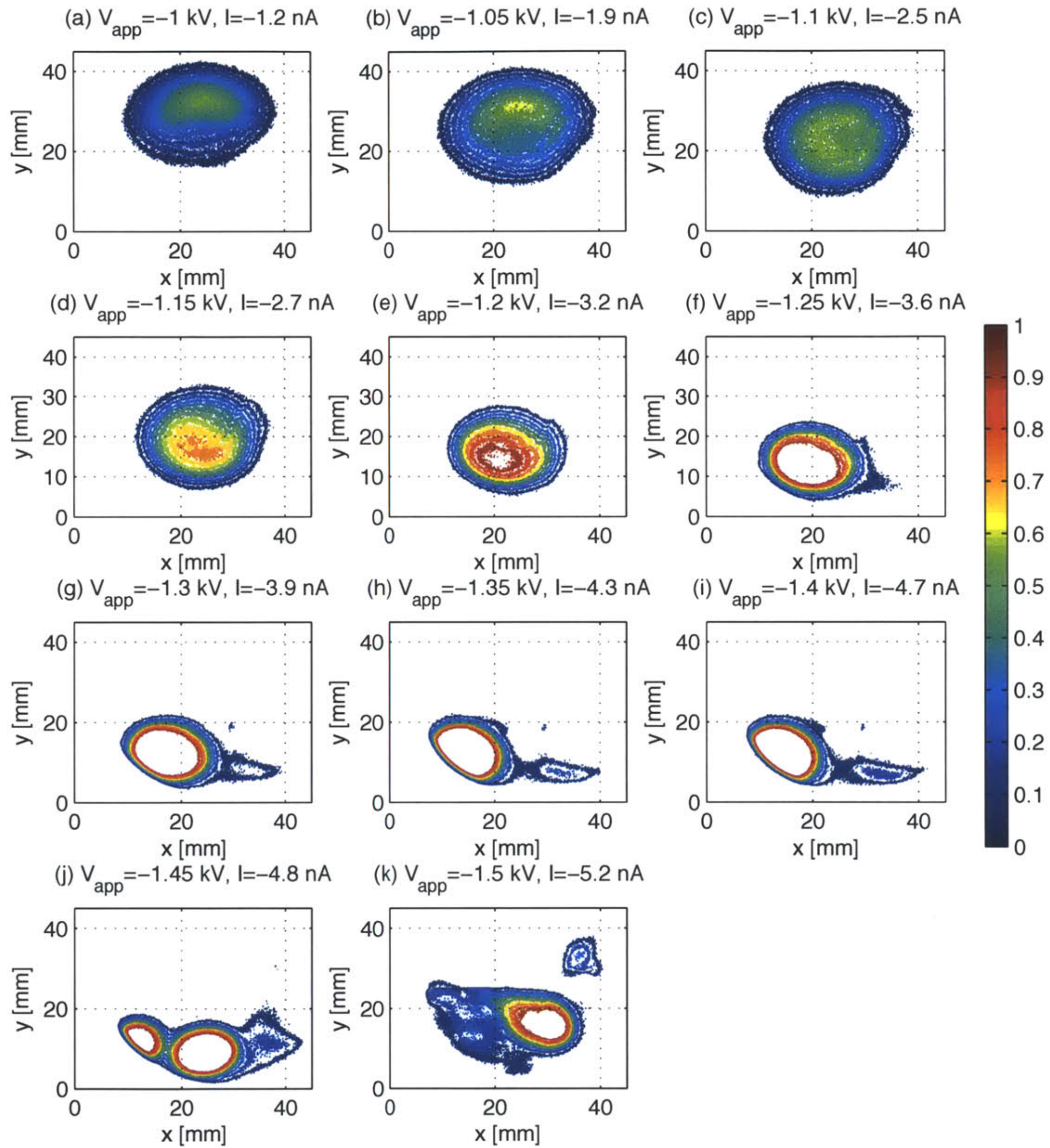

Figure 4-5: (a)-(k) Beam profiles for emitter voltages from $V_{app} = -1$ kV to $V_{app} = -1.5$ kV

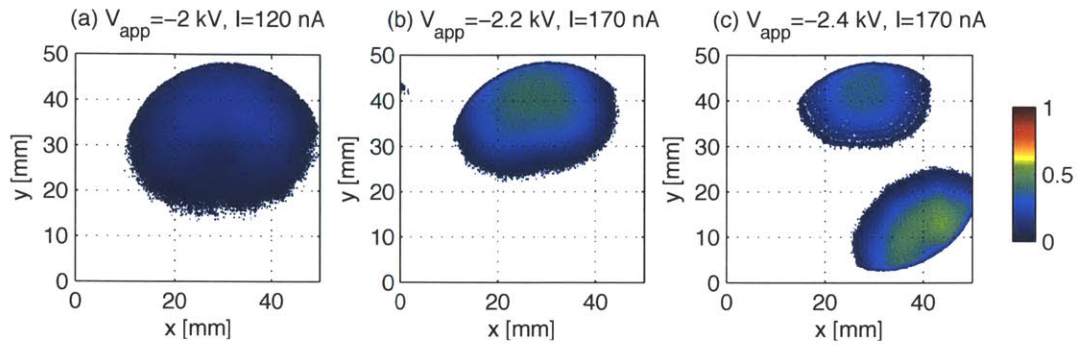

Figure 4-6: Beam profiles for different emitter voltages for a larger R_c tip

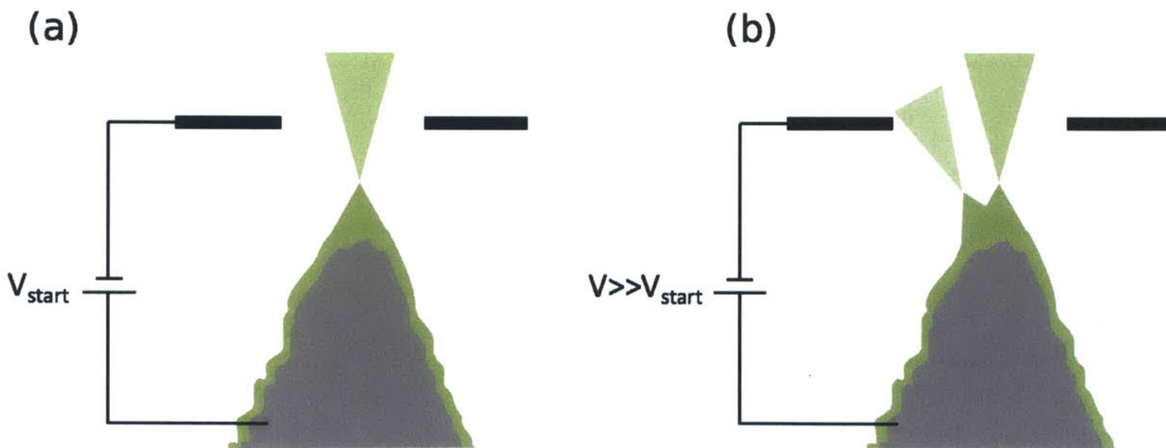

Figure 4-7: Diagram of emitter with Taylor cone at (a) Starting voltage (b) Voltages for which multiple cones can be sustained

surface as we are using a perfectly conducting emitter and a conductive liquid and, if the tip is locally rough at its apex, the small protrusions could serve as electric field amplifiers and lead to the formation of Taylor cones at places other than the tip apex.

4.2 Neutral Beam Visualization

To determine the distribution of the neutral particle population within the beam, we operate the source at $V_{app} = \pm 1.35$ kV with a 10 second period and apply a deflection voltage $V_{DEF} = 1.5$ kV on every other period of the emitter. The gain of the viewing system is increased by setting $V_{MCP} = 1.8$ kV and $V_P = 5$ kV. The full beam profiles for the positive and negative polarity are shown in Fig. 4-8 (a) and (b), respectively. The images of the deflected beam are shown in Figs. 4-8 (c) and (d), for the positive and the negative polarity. Each image is the average of 20 frames taken every 0.2 s in order to reduce noise.

From Figs. 4-8(c) and (d) we note that the charged particles in the beam have been redirected due to the deflector action. In Fig. 4-8(c), the circular impact observed should correspond to neutral particles that were unaffected by the applied electric field. The neutral population profile is centered at the same position as the non-deflected beam, and is more intense at the center. In the negative mode, Fig. 4-8(d), we see that the beam is deflected, but it is not possible to completely isolate the neutral signal from the beam. This might be due to the beam being inclined with respect to the deflection grids' central axis, which could result in poor deviation of the negative mode. It is also possible that the ions in the beam are fragmenting as the beam crosses the deflector, in which case the resulting neutral particles could yield a signal inbetween the neutral impact and the deflected beam impact.

Results from a similar experiment are shown in Fig. 4-9. The source operates at $V_{app} = \pm 1.25$ kV with a 10 second period, and we increase the deflection voltage to $V_{DEF} = 2$ kV. The viewing system settings are $V_{MCP} = 1.8$ kV and $V_P = 5$ kV. The full beam profile for the positive and negative polarity are shown in Fig. 4-9 (a) and

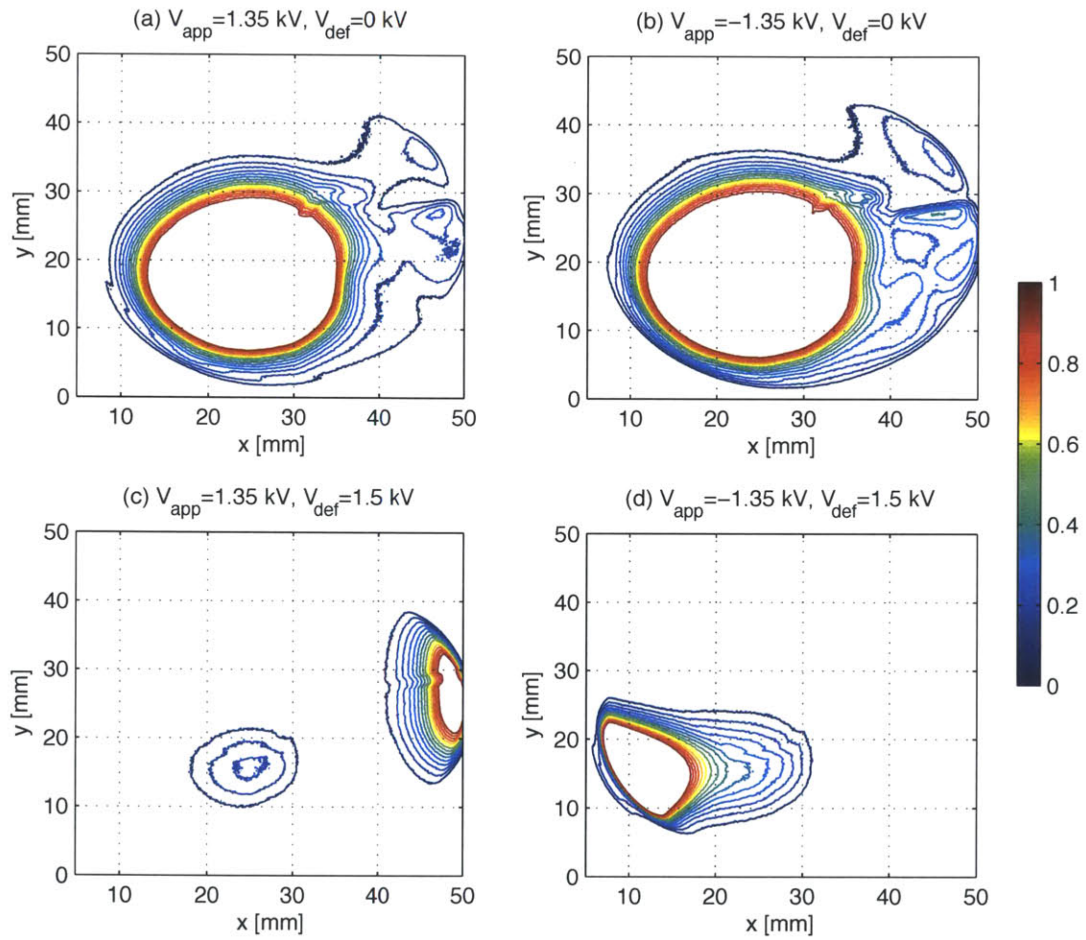

Figure 4-8: (a and b) Undeflected beam profiles (c and d) Profiles of neutral particles and deflected beam.

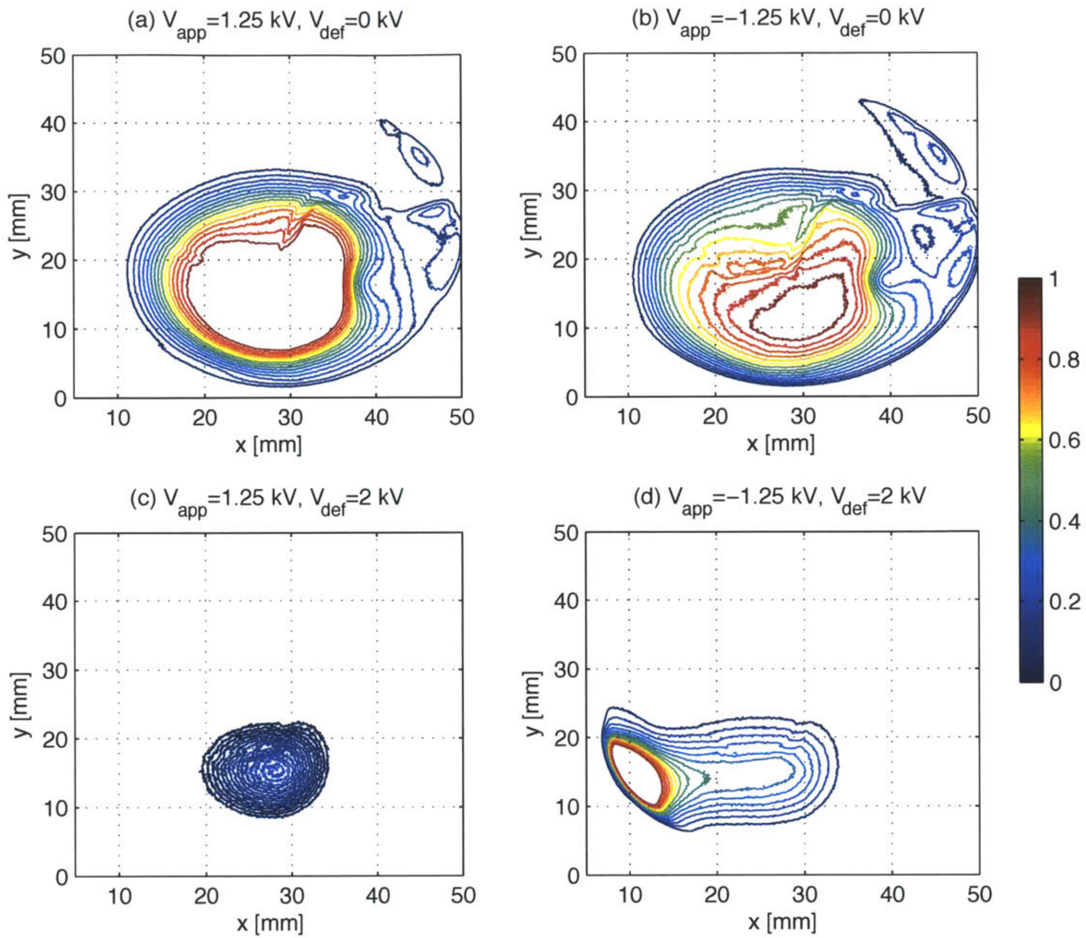

Figure 4-9: (a and b) Undeflected beam profiles (c and d) Profiles of neutral particles and deflected beam.

(b), respectively, and their corresponding deflected profiles are shown in Figs. 4-9 (c) and (d). Each image is the average of 20 frames taken every 0.2 s, as in Figure 4-8.

In this trial we also see that the charged particles in the beam are deviated by the deflecting voltage. In the positive mode (Fig. 4-9 (c)), the neutral profile is isolated from the ion signal; the distribution shows clearly how most of the neutral population is located close to the center of the beam. In the negative mode (Fig.4-9 (d)), even at the higher deflection voltage and lower beam energy, it is still not possible to completely isolate the neutral signal. Nonetheless, we can infer that most of the neutral signal persists close to the center of the beam.

The neutral population signal on the BVS can also be observed in experiments

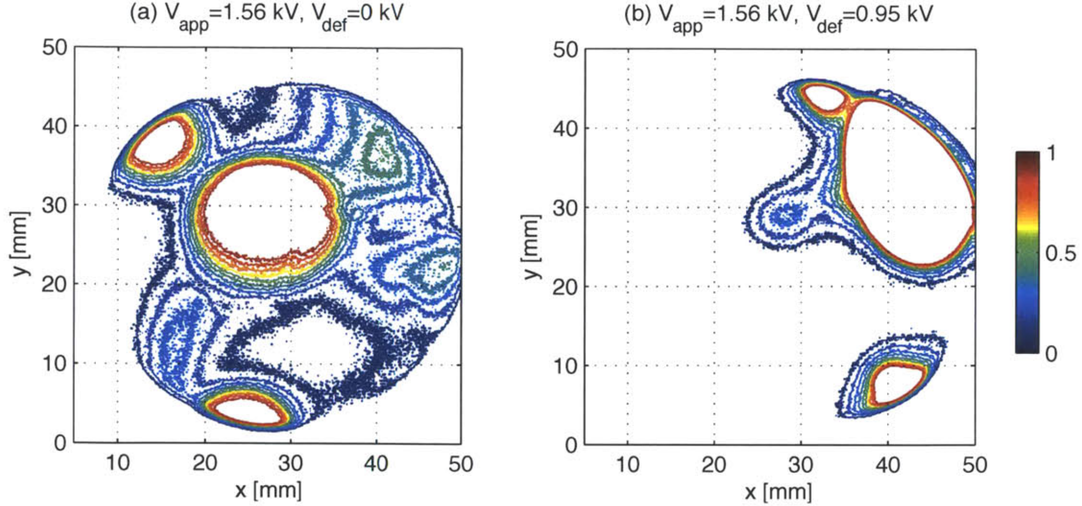

Figure 4-10: (a) Undeflected beam profile of a multiple cone emission (b) Multiple beams are deflected and neutral signal observed

where the source is producing multiple beams. Fig. 4-10 shows the undeflected and deflected beams of the source operating at $V_{app} = 1.56$ kV (These images are single snapshots of the beam). We can observe multiple cone signals in the visualization area when there is no deflection and, if we apply a bias $V_{DEF} = 0.95$ kV to the deflector plate, we can observe how the individual beams are deflected to the side of the visualization area, with the neutral signal of the center beam clearly appearing at the beam's original position. The signal from the neutral impact is weak in this experiment, and so we have set $V_{MCP} = 2$ kV and $V_P = 5$ kV to maximize the intensity of the neutral particle signal in the visualization system. This experiment also indicates that the neutral population must be concentrated at the center of the beam.

4.3 Retarding Potential Analysis

As mentioned previously, we would like to estimate the amount of fragmentation occurring in the neutral visualization experiments, and so we perform RPA analysis on the tip used for the voltage sweep experiments and the neutral visualization experiments. For these experiments, the tip was positioned approximately 1 mm away from

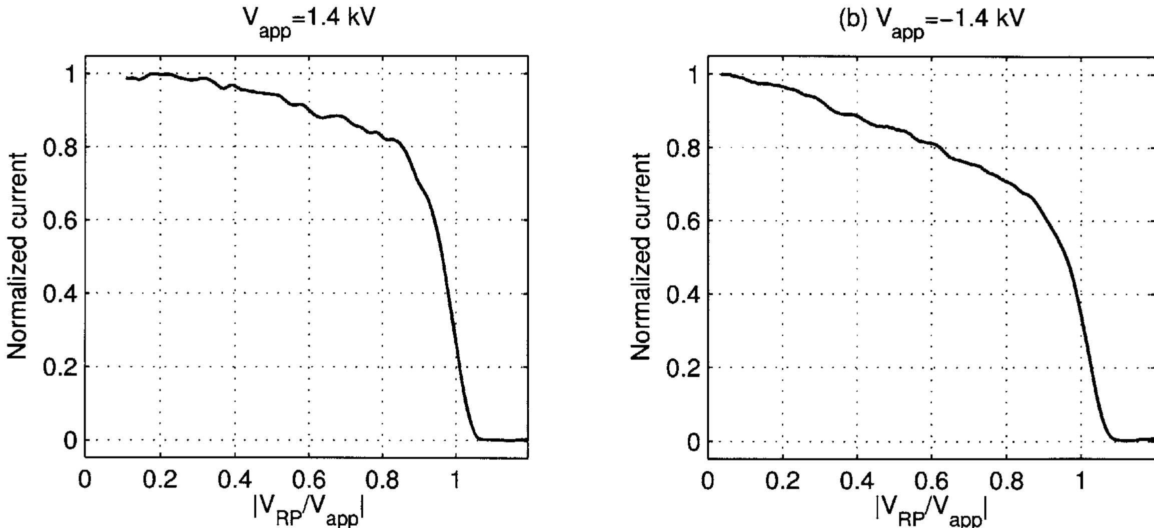

Figure 4-11: Retarding Potential Analyzer Curves for $V_{app} = \pm 1.4$ kV

the extractor, and the ILIS startup potential was found to be close to +/- 1.38 kV. In addition, we place the RPA detector close enough to the extractor that the full beam is captured for the energy analysis.

We measure the energy distribution of the full beam emitted at an applied potential of $V_{app} = \pm 1.4$kV, and the collected current as a function of the retarding potential is shown in Fig. 4-11. This energy curve is a low-resolution measure of the beam energy distribution because there are two artifacts in the data provoked by the instrument: (1) artificial spreading in the energy signal due to beam divergence and (2) potential sagging, explained below. The purpose of these experiments is not to determine the precise energy characteristics of our source, but rather to estimate the level of ion fragmentation (hence, neutral production) for a source operating in the conditions used for the neutral visualization experiments, which is possible despite these effects.

1. **Spreading**. Previous studies indicate that the beam emitted from an EMI-BF_4-based ILIS has a half aperture angle of approximately 18° [17], i.e, an ion can approach the retarding grids at an angle θ between 0° and 18°. An ion with energy qV_0 should ideally be stopped by a potential barrier $V_{RP} = V_0$. However, an ion coming at an angle θ will be deflected by a potential $V_{RP} = V_0 \cos^2 \theta$.

Then, since the RPA instrument is capturing the whole beam, it should be expected to see current decreases for a range of energies, even if the ions come with a sharp energy distribution. In Fig. 4-11, we do not observe a sharp drop in beam current close to the applied potential, but rather a gradual decrease; the actual energy spread of the population coming close to the applied potential is sharper than what is measured, as was shown before [19, 16].

2. **Sagging**. It can be observed that the amplitude of the measured current does not drop to zero for the retarding potentials exceeding the applied potential; the emission potential must be exceeded by roughly 100 V before no current passes. The retarding grids should create deep equipotential regions along the path of the beams, but this RPA uses coarse grids that do not provide a uniform potential. Then, even if the grid material is at the retarding potential, some intermediate regions can be at lower voltages, which allow some of the ions to leak to the collector even if they have energies less than V_{RP}.

The RPA data shown in Fig. 4-11 is used to estimate the fraction of the current resulting from break-up events. This can be explained as follows: ideally, for a monoenergetic beam, all the ions are moving with a kinetic energy equal to their applied acceleration energy, so when the retarding potential matches the applied voltage, we should see a sharp drop in the collected current. These drops can be distinguished in Fig. 4-11. However, if ion breakup happens after acceleration, the resulting ions have a fraction of their initial kinetic energy, and so there will be current drops, or steps, in the RPA signal. Furthermore, breakup can happen in the acceleration zone, between the emitter and the extractor, and so ions can have a continuum of energies as predicted by equation (2.32). This phenomena gives rise to a continuous current drop in the RPA signal as the retarding potential is increased. The fraction of the collected current that results from breakup events is then the current collected between $V_{RP} = 0$ kV and $V_{RP} = V_{app}$, which is approximately 20 % for the positive mode and 30 % for the negative mode.

Chapter 5

Conclusions and Future Work

5.1 Implications of characterization results

The visualization results obtained in this thesis indicate that ILIS have stable output when operating in alternating polarity, as the beam does not change its position when the polarity is reversed. In addition, we have determined that the source operates stably close to the emission onset potential, but transitions from single to multiple beam operation as the potential is increased.

For FIB, it is required for the source to have a single, stable beam for optimal focusing. The multiple beam regime of ILIS is not suitable for FIB and, although the source could be operated close to the onset potential, it is desirable for the tip to be able to operate stably at a larger range of voltages, so that the energy of the ions could be adjusted or to increase the extracted current.

The multiple beam operation could be mitigated by modifying the emitter surface. The surface of an ILIS is roughened to enable the liquid to reach the tip, which for a perfectly smooth emitter, would be inaccessible due to the adverse pressure gradient created by the smaller radius of curvature as we approach the apex. However, if the roughening is finer than the radius of curvature of the tip, the tip effectively has several protrusions. These protrusions amplify the electric field and lead to multiple beam emission at the increased extraction voltages. If the tip were to be modified so that it was locally smooth at the apex, but rough up to a distance comparable

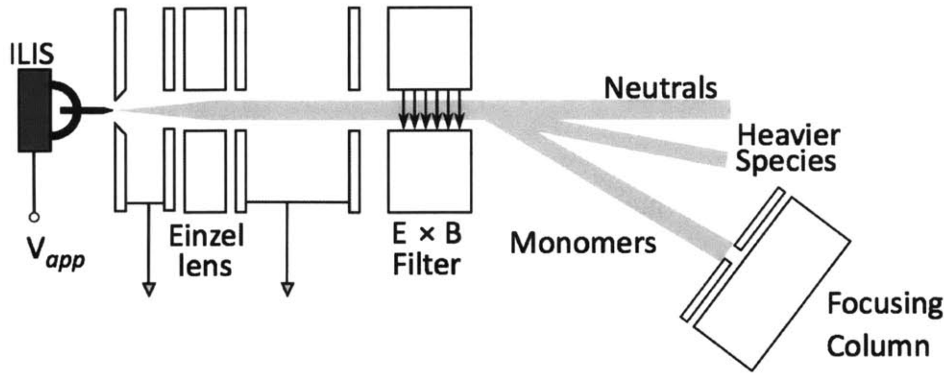

Figure 5-1: Schematic of possible filtering setup for ILIS FIB implementation

to the emitter radius of curvature, the transition to multiple beam behavior could be suppressed. Furthermore, such a modification could guarantee that the beam is always fired in the same direction.

We have also demonstrated that most of the neutral population of an ILIS beam is concentrated at the center of the beam. To realize an ILIS-based FIB with the smallest probe size possible, it would be necessary to select the monoenergetic component of the beam and eliminate the neutral particles using a Wien (E×B) filter. A possible scheme is illustrated in Fig. 5-1. The beam produced by an ILIS would be initially collimated using an Einzel lens, and the prefocused beam would then pass through the Wien filter. This filter creates perpendicular electric and magnetic fields along the beam path. As the multiple ion species pass through the filter, all ions are deflected while the neutrals are unaffected. The lightest ions (i.e. the monomers) will be deflected most due to the magnetic field. By selecting only the deflected monomers into a focusing column with a limiting aperture, we eliminate the neutrals present in the center of the beam as well as those that could result from break-up of heavier ions. This scheme also gives an additional advantage, as the monomers selected for focusing could potentially have an energy distribution with a smaller energy spread than that of the full beam. This energy spread reduction would reduce chromatic aberrations and lead to finer probe sizes.

5.2 Distal Electrode Configurations for long lifetime

In the introduction, it was mentioned that ion sources must have lifetimes on the order of hundreds of hours in order to be viable for FIB utilization. ILIS operation in a single polarity for tens of hours has been demonstrated using a new distal electrode configuration [1]. This configuration still needs to be characterized, but it offers key advantages over traditional ILIS operation.

Until recently, ILIS operation in a single polarity for more than a few minutes was impractical due to electrochemical decomposition of the liquid. As ions of a single polarity are drawn from the ILIS, the accumulation of the counter ions on the surface of the electrode leads to the formation of a charge double layer, across which electron transfer can occur, leading to reactions and emission degradation within a few minutes. The decomposition of the liquid can be avoided by alternating the polarity of the source to avoid the formation of the charged layer. ILIS operation for 200 hours was demonstrated by Lozano and Martinez-Sanchez in 2004 [15], with the source operating in alternating polarity at a frequency of 1 Hz.

Although the ILIS operating in an alternating polarity mode has an adequate lifetime, it might not be suitable for FIB. ILIS produce different ion species on each polarity and for FIB, if a particular species were desired for patterning a sample (for instance, I^-), it would be best to operate the source in a single polarity continuously. If voltage alternation were required to avoid electrochemical decomposition of the source, the beam would have to be blanked every other half period in order to expose the sample to only the desired species. Then, the required patterning time would be doubled; considering a typical FIB process might take tens of minutes to a few hours, the need for blanking might make the processing time excessively long for some applications.

The use of a distal electrode configuration can mitigate the electrochemical degradation of an ILIS in single polarity operation and thus provide a long-lifetime ILIS suitable for FIB. The distal electrode configuration is shown in Fig. 5-2. As usual, the

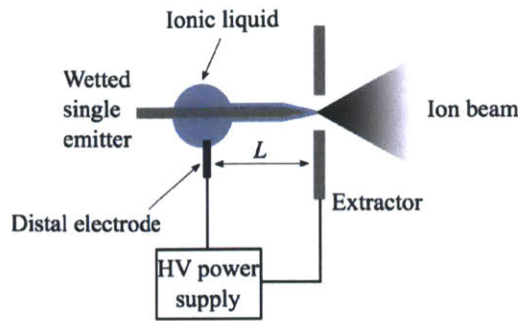

Figure 5-2: ILIS with the distal electrode configuration. From [1]

emitter is an externally wetted needle, but the emitter is electrically floating while the voltage is applied by an upstream distal electrode that makes "electrical contact exclusively with the conductive liquid" [1]. In this way, the double layer responsible for electrochemistry forms on the distal electrode, far from the emission site, and, if any corrosion occurs, it occurs upstream from the emission site. This configuration was tested in the positive mode on an externally wetted tungsten ILIS for 76 hours, with stable current emission and no signs of degradation on the emitter [1].

Then, for FIB, we would implement ILIS with distal electrode contacts. However, the long-lifetime behavior of ILIS operating in this alternative configuration still needs to be characterized thoroughly. Future work will aim to measure current fluctuations, beam composition and beam energy over extended periods, to ensure that any potential decomposition reactions do not affect the emission process. Furthermore, direct visualization of the beam over prolonged operation will determine if the beam stays in the same location, which is necessary for FIB implementation.

5.3 The road to an ILIS-based FIB

ILIS are a very promising option for FIB, but several research efforts must be performed to guarantee their reliable operation in a focusing column, as well as to determine the ultimate limits of the technology.

In the near term, an emitter that is not prone to multiple beam emission and that maintains a constant supply of liquid to the apex of the emitter should be

developed. Once such an emitter is obtained, it should be tested with the distal electrode configuration to characterize the long-lifetime behavior of the source and determine the maximum operation lifetime. This research should be performed for several ionic liquids, in order to characterize a range of ion species that could be used for FIB. Further research would include filtration of the ILIS beam and measurements of the energy spread of the mono energetic monomers. Knowledge of this energy spread would allow estimation of the ultimate probe sizes attainable with an ILIS FIB.

The filtered beam of monomers from the improved ILIS can then be directed towards an optical column for focusing. First steps would aim at measuring the probe size for a fixed set of lens parameters, which can then be used to estimate the source brightness more accurately. The fine probes of ILIS ions can then be used to study several applications. For instance, it would be adequate to study the etching effects of ILIS on materials that are hard to process using trad itional techniques (such as GaN, SiGe and graphene). ILIS beams could also be advantageous for applications like secondary ion mass spectrometry, where the large sputtering yield would improve the signals required for chemical analysis. The variety of ion species provided by ILIS, along with possibility to provide both positive and negative ion beams with nanometer resolution, gives a whole new set of possibilities for processing and analysis of materials at the nanometer scale.

Bibliography

[1] Natalya Brikner and Paulo C. Lozano. The role of upstream distal electrodes in mitigating electrochemical degradation of ionic liquid ion sources. *Applied Physics Letters*, 101(19):193504, 2012.

[2] S. Castro and J. Fernandez de la Mora. Effect of tip curvature on ionic emissions from Taylor cones of ionic liquids from externally wetted tungsten tips. *Journal of Applied Physics*, 105(3):034903, 2009.

[3] Conrad Escher, Sandra Thomann, Cornel Andreoli, Hans-Werner Fink, Julien Toquant, and Dieter W. Pohl. Vacuum ion emission from solid electrolytes: An alternative source for focused ion beams. *Applied Physics Letters*, 89(5):053513, 2006.

[4] W. H. Escovitz, T. R. Fox, and R. Levi-Setti. Scanning transmission ion microscope with a field ion source. *Proceedings of the National Academy of Sciences of the United States of America*, 72(5):1826–1828, 1975.

[5] Timothy P. Fedkiw. *Characterization of an iodine-based ionic liquid ion source and studies on ion fragmentation.* PhD thesis, Massachusetts Institute of Technology, 2010.

[6] Timothy P. Fedkiw and Paulo C. Lozano. Development and characterization of an iodine field emission ion source for focused ion beam applications. In *Journal of Vacuum Science & Technology B*, volume 27, pages 2648–2653. AVS, 2009.

[7] Juan Fernandez de la Mora. The Fluid Dynamics of Taylor Cones. *Annual Review of Fluid Dynamics*, 39:217–243, January 2007.

[8] Toshiaki Fujii, Koji Iwasaki, Masanao Munekane, Toshitada Takeuchi, Masakatsu Hasuda, Tatsuya Asahata, Masahiro Kiyohara, Toshiharu Kogure, Yukimitsu Kijima, and Takashi Kaito. A nanofactory by focused ion beam. *Journal of Micromechanics and Microengineering*, 15(10):S286, 2005.

[9] Jacques Gierak. Focused ion beam technology and ultimate applications. *Semiconductor Science and Technology*, 24(4):43001, 2009.

[10] S. K. Guharay, E. Sokolovsky, and J. Orloff. Characteristics of focused beam spots using negative ion beams from a compact surface plasma source and merits for new applications. *Journal of Vacuum Science & Technology B: Microelectronics and Nanometer Structures*, 16(6):3370, November 1998.

[11] F. J. Higuera. Model of the meniscus of an ionic-liquid ion source. *Physical Review E*, 77(2):1–11, February 2008.

[12] R. Hill, J. Notte, and L. Scipioni. Scanning Helium Ion Microscopy. In *Advances in Imaging and Electron Physics*, volume 170, pages 65–148. Elsevier Inc., 2012.

[13] C. Larriba, S. Castro, J. Fernandez de la Mora, and P. Lozano. Monoenergetic source of kilodalton ions from Taylor cones of ionic liquids. *Journal of Applied Physics*, 101(8):084303, 2007.

[14] C. Larriba, D. Garoz, C. Bueno, S. Castro, J. Fernandez de la Mora, Y. Yoshida, G. Saito, R. Hagiwara, K. Matsumoto, and J. Wilkes. Taylor Cones of Ionic Liquids as Ion Sources: The Role of Electrical Conductivity and Surface Tension. In *ACS Sympsium Series: Ionic Liquids IV*, chapter Chapter 21, pages 308–319. American Chemical Society, 2007.

[15] Paulo Lozano and Manuel Martínez-Sánchez. Ionic liquid ion sources: suppression of electrochemical reactions using voltage alternation. *Journal of Colloid and Interface Science*, 280(1):149–154, 2004.

[16] Paulo Lozano and Manuel Martinez-Sanchez. Efficiency Estimation of EMI-BF4 Ionic Liquid Electrospray Thrusters. In *Proceedings of the 41 st AIAA/ASME/SAE/ASEE Joint Propulsion Conference*, number July, 2005.

[17] Paulo Lozano and Manuel Martínez-Sánchez. Ionic liquid ion sources: characterization of externally wetted emitters. *Journal of Colloid and Interface Science*, 282(2):415–421, 2005.

[18] Paulo C. Lozano. *Studies on the ion-droplet mixed regime in colloid thrusters.* PhD thesis, Massachusetts Institute of Technology, 2003.

[19] Paulo C. Lozano. Energy properties of an EMI-Im ionic liquid ion source. *Journal of Physics D: Applied Physics*, 39(1):126–134, January 2006.

[20] Manuel Martinez-Sanchez. 16.522 Space Propulsion Lecture Notes: Colloidal Engines, 2004.

[21] Joachim Mayer, Lucille A. Giannuzzi, Takeo Kamino, and Joseph Michael. TEM Sample Preparation and Damage. *MRS Bulleting*, 32(May):400–407, 2007.

[22] Jon Orloff. Review Article: focused ion beams. *Rev. Sci. Instrum.*, 64(5):1105–1130, 1993.

[23] Jon Orloff and Lynwood Swanson. Fine focus ion beams with field ionization. *Journal of Vacuum Science and Technology*, 15(3):845–848, 1978.

[24] Jon Orloff, Mark Utlaut, and Lynwood Swanson. *High Resolution Focused Ion Beams.* Kluwer Academic/Plenum Publishers, New York, 2002.

[25] Carla Perez-Martinez, Stephane Guilet, Jacques Gierak, and Paulo Lozano. Ionic liquid ion sources as a unique and versatile option in FIB applications. *Microelectronic Engineering*, 88(8):2088–2091, 2011.

[26] Carla Perez-Martinez, Stephane Guilet, Noelle Gogneau, Pascale Jegou, Jacques Gierak, and Paulo Lozano. Development of ion sources from ionic liquids for microfabrication. *Journal of Vacuum Science Technology B: Microelectronics and Nanometer Structures*, 28(3):L25 –L27, May 2010.

[27] Carla S. Perez-Martinez and Paulo C. Lozano. Visualization of beams from ionic liquid ion sources for focused ion beam applications. *Journal of Vacuum Science & Technology B: Microelectronics and Nanometer Structures*, 30(6):06F601, 2012.

[28] I. Romero-Sanz, R. Bocanegra, J. Fernandez de la Mora, and M. Gamero-Castano. Source of heavy molecular ions based on Taylor cones of ionic liquids operating in the pure ion evaporation regime. *Journal of Applied Physics*, 94(5):3599, 2003.

[29] L. Scipioni, D. Stewart, D. Ferranti, and A. Saxonis. Performance of multicusp plasma ion source for focused ion beam applications. *Journal of Vacuum Science & Technology B: Microelectronics and Nanometer Structures*, 18(6):3194, 2000.

[30] N. S. Smith, W. P. Skoczylas, S. M. Kellogg, D. E. Kinion, P. P. Tesch, O. Sutherland, a. Aanesland, and R. W. Boswell. High brightness inductively coupled plasma source for high current focused ion beam applications. *Journal of Vacuum Science & Technology B: Microelectronics and Nanometer Structures*, 24(6):2902, 2006.

[31] Geoffrey Taylor. Desintegration of Water Drops in an Electric Field. *Proceedings of the Royal Society A*, 280(1382):383–397, July 1964.

[32] V. N. Tondare. Quest for high brightness, monochromatic noble gas ion sources. *Journal of Vacuum Science & Technology A: Vacuum, Surfaces, and Films*, 23(6):1498, 2005.

[33] Ampere Tseng. Recent developments in nanofabrication using focused ion beams. *Small*, 1(10):924–39, October 2005.

[34] Ivo Utke, Patrik Hoffmann, and John Melngailis. Gas-assisted focused electron beam and ion beam processing and fabrication. *Journal of Vacuum Science & Technology B: Microelectronics and Nanometer Structures*, 26(4):1197, 2008.

[35] Bill W. Ward, John A. Notte, and Nicholas P. Economou. Helium ion microscope: A new tool for nanoscale microscopy and metrology. *Journal of Vacuum Science & Technology B: Microelectronics and Nanometer Structures*, 24(6):2871, 2006.

[36] Donald Winston, Vitor R. Manfrinato, Samuel M. Nicaise, Lin Lee Cheong, Huigao Duan, David Ferranti, Jeff Marshman, Shawn McVey, Lewis Stern, John Notte, and Karl K. Berggren. Neon Ion Beam Lithography (NIBL). *Nano Letters*, 11(10):4343–7, 2011.

[37] Anthony N. Zorzos and Paulo C. Lozano. The use of ionic liquid ion sources in focused ion beam applications. In *Journal of Vacuum Science & Technology B*, volume 26, pages 2097–2102. AVS, 2008.